Monthly Notices of the Royal Astronomical Society
MNRAS **470,** 1593–1611 (2017) doi:10.1093/mnras/stx1237

An infrared photometric and spectroscopic study of post-AGB stars

V. Venkata Raman,[1⋆] B. G. Anandarao,[1⋆] P. Janardhan[1] and R. Pandey[2]
[1] *Physical Research Laboratory (PRL), Navrangpura, Ahmedabad 380009, India*
[2] *Physics Department, M.L.S. University, Udaipur, India*

Accepted 2017 May 18. Received 2017 May 17; in original form 2016 March 3

ABSTRACT

We present here *Spitzer* mid-infrared (IR) spectra and modelling of the spectral energy distribution (SED) of a selection of post-asymptotic giant branch (PAGB) stars. The mid-IR spectra of the majority of these sources showed spectral features such as polycyclic aromatic hydrocarbons (PAHs) and silicates in emission. Our results from SED modelling showed interesting trends of dependence between the photospheric and circumstellar parameters. A trend of dependence is also noticed between the ratios of equivalent widths (EWs) of various vibrational modes of PAHs and the photospheric temperature T_* and model-derived stellar parameters for the sample stars. The PAGB mass-loss rates derived from the SED models are found to be higher than those for AGB stars. In a few objects, low- and high-excitation fine-structure emission lines were identified, indicating their advanced stage of evolution. Further, IR vibration modes of fullerene (C_{60}) were detected for the first time in the PAGB star IRAS 21546+4721.

Key words: techniques: spectroscopic – stars: AGB and post-AGB – circumstellar matter – stars: evolution – stars: mass-loss – dust, extinction.

1 INTRODUCTION

Post-asymptotic giant branch (PAGB) stars or protoplanetary nebulae (PPNe) represent a short-lived, rapidly varying and little-understood phase during the evolution of intermediate-mass stars towards the planetary nebula (PN) stage (van Winckel 2003; Kwok 2007 and references therein). The evolutionary phases of PAGB and PPNe are nearly indistinguishable and from here onwards we treat the two to be the same. These sources exhibit infrared excess and molecular line emission from dust and molecules in the circumstellar envelopes formed by mass loss during the asymptotic giant branch (AGB) phase. Circumstellar dust in PAGB stars causes significant extinction in the visible region. The exact composition of circumstellar dust grains is still a matter of debate (e.g. see Cerrigone et al. 2009; Zhang, Kwok & Hrivnak 2010). The evolution during the PAGB phase can be identified by several spectroscopic signatures – from molecular hydrogen emission to atomic hydrogen recombination lines, as well as forbidden transitions from several atoms and ions. Further, the onset of UV radiation can also be inferred from the detection of circumstellar polycyclic aromatic hydrocarbons (PAHs), which are excited by absorption of soft UV radiation in carbon-rich PAGB stars (e.g. Kwok 2004; Tielens 2005). Investigation of circumstellar matter and chemical synthesis can therefore help in probing and understanding the early stages of PN formation.

Pioneering studies on the infrared spectra of PAGB stars were made and reported by Kwok, Volk & Hrivnak (1999), Hrivnak, Volk & Kwok (2000) and references therein, with particular emphasis on PAH features and other as yet unidentified features as well as on molecular hydrogen lines (e.g. Kelly & Hrivnak 2005 and references therein). In the present study, we model the SEDs for a fairly large sample of PAGB stars using the available archival data covering the visible to far-infrared regions. We then endeavour to find whether the model-derived circumstellar parameters indicate a possible dependence on evolution of the objects.

The sample selection of PAGB stars used in the present study is described in Section 2. In Section 3 we present mid-IR spectra of the sample sources. In Section 4 we present modelling of SEDs and in Section 5 we discuss the possible correlation between the circumstellar and photospheric parameters obtained from the SED models and also between the various PAH modes of vibration with the evolution of the central star. In Section 6 we identify a few transition objects in our sample through the detection of low- and high-excitation fine-structure lines in the mid-IR spectra. In Section 7 we present the detection of fullerenes in one of the sample PAGB stars. In Section 8 we summarize the conclusions of the present work.

2 SAMPLE OF PAGB STARS AND PHOTOMETRIC ARCHIVAL DATA

The sample of PAGB stars studied was selected from Szczerba et al. (2007). Based on their *JHK*-band magnitudes being brighter than 13–14, a total of about 71 PAGB stars were identified for the present

⋆ E-mail: vvenkat@prl.res.in (VVR); anand@prl.res.in (BGA)

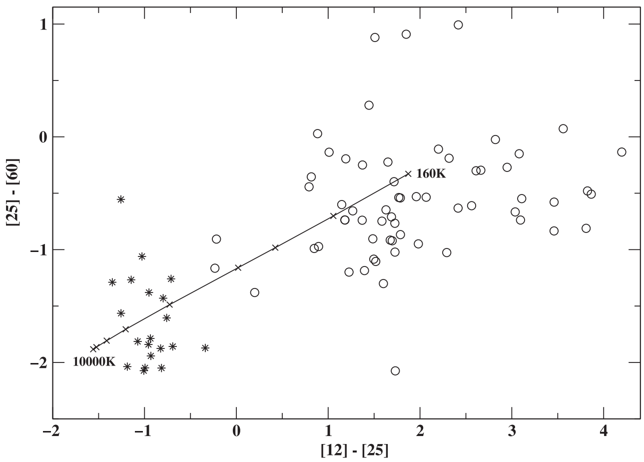

Figure 1. IRAS colour–colour diagram for the stars in our sample. PAGB stars (open circles) occupy positions that have very cool circumstellar shells. The AGB stars (asterisks) from Venkata Raman & Anandarao (2008) are also shown for comparison. The crosses along the line represent blackbody temperatures of 10000, 5000, 2000, 1000, 500, 300, 250, 200 and 160 K (see van der Veen & Habing 1988) in the colour–colour space.

study. From the classification scheme based on the IRAS [25–60] versus [12–25] colour–colour diagram (shown in Fig. 1; see van der Veen & Habing 1988), it is clear that the objects selected for the present study are much more evolved than the sources in their AGB phase considered in our earlier work (Venkata Raman & Anandarao 2008). Spectral types for a number of PAGB candidates were taken from SIMBAD. For some of the objects without spectral type information from SIMBAD, we have used the spectral classification from the optical survey of Suarez et al. (2006). Some of the objects in the selected PAGB star samples are identified as 'transition objects' by Suarez et al. (2006). It may be noted that small (and in some cases, large) differences exist in the spectral types of some common objects between SIMBAD and Suarez et al. (2006).

The photometric data required for constructing the SEDs in the entire visible to far-infrared region were obtained from several archives. The data were obtained from the following sources: visible *UBVRI* photometry from the VIZIER archives; the near-IR *JHK* bands from the 2MASS archive (Skrutskie et al. 2006); the mid-infrared from the Midcourse Space Experiment (MSX) bands at 8.3, 12.1, 14.7 and 21.3 μm (Egan, Price & Kraemer 2003); the 3.6-, 4.5-, 5.8- and 8-μm bands from IRAC–*SPITZER* (Benjamin et al. 2003); the mid-infrared bands at 9 and 18 μm and far-infrared bands centred around 65, 90, 140 and 160 μm from the extensive all-sky survey from *AKARI* (Ishihara, Onaka & Kataza 2010); finally, the 12-, 25-, 60- and 100-μm band data were obtained from *IRAS* (Helou & Walker 1988) archives.

3 *Spitzer* SPECTRA OF PAGB OBJECTS

Spitzer public archival spectroscopic data from the InfraRed Spectrograph (IRS) on board the *Spitzer* Space Telescope covering the mid-IR region between 5.2 and 38 μm (Houck et al. 2004) were used for most of the sample stars in our present study. Most of the data used here were from the short–low (SL) and long–low (LL) modules covering 5.13–14.29 and 13.9–39.9 μm respectively. For a few sources, the short–high (SH: 9.89–19.51 μm) and long–high (LH: 18.83–37.14 μm) modules were also used.

The basic calibrated data (BCD) and post-BCD data from the *Spitzer* archive were analysed using the Spectroscopic Modelling Analysis and Reduction Tool (SMART) and *Spitzer* IRS Custom Extraction (SPICE) software packages, respectively. The highly processed data products (HPDP) from the *ISO* archive (Sloan et al. 2003) were used for a few sources in our list for which *Spitzer* data were not available.

Based on identified mid-IR spectral features, we classified our sample PAGB stars as those having (i) strong/weak or blended PAH features, (ii) silicate emission, in some cases along with PAH features, (iii) silicate absorption, (iv) a prominent broad bump around 11 μm with no PAH features and (v) nearly featureless spectra. The blended PAH refers to the blend of two or more neighbouring PAH lines to form a single broad feature. Similar classification based on the presence of PAH (C-rich), silicate (O-rich) and a combination of PAH and silicate features was performed by Cerrigone et al. (2009). In addition to Cerrigone et al's classification, the present study identifies objects that have silicate absorption, those with a 11-μm bump and thirdly those with featureless spectra. Table 1 provides the list

Table 1. Source of spectra and dust classification of the PAGB objects.

Object name	Source of spectra	Dust classification
01005+7910	*Spitzer* SL, LL, SH	PAH
04296+3429	*Spitzer* SL, SH, LH	PAH
05089+0459	*Spitzer* SH	Not classified
05113+1347	*Spitzer* SH	PAH
05341+0852	*Spitzer* SH, LH	PAH
06034+1354	*Spitzer* SH, LH	Sil emission
06530−0213	*Spitzer* SH, LH	PAH
06556+1623	*Spitzer* SL, LL	Not classified
07134+1005	*Spitzer* SH, ISO	PAH
08005−2356	*Spitzer* SH, LH	11-micron source
08335−4026	*Spitzer* SL, LL	PAH+Sil
10211−5922	*Spitzer* SL, SH, LH	Sil emission
11201−6545	*Spitzer* SL, SH, LH	Sil emission
11339−6004	*Spitzer* SL, SH, LH	11-micron source
11353−6037	*Spitzer* SL, SH, LH	PAH+Sil
11387−6113	*Spitzer* SL, SH, LH	PAH+Sil
12145−5834	*Spitzer* SL, LL	PAH
13245−5036	*Spitzer* SL, LL	Not classified
13313−5838	*Spitzer* SL, LL	PAH
13500−6106	*Spitzer* SL, SH, LH	Sil absorption
13529-5934	*Spitzer* SL, SH, LH	Not classified
14325−6428	*Spitzer* SL, SH, LH	11-micron source
14341−6211	*Spitzer* SL, SH, LH	11-micron source
14346−5952	*Spitzer* SH, LH	Not classified
14429−4539	*Spitzer* SL, SH, LH	PAH
14482−5725	*Spitzer* SL, LL	PAH+Sil
15482−5741	*Spitzer* SL, LL	PAH
16206−5956	*Spitzer* SL, SH, LH	Sil emission
16494−3930	*Spitzer* SH, LH	11-micron source
16559−2957	*Spitzer* SL, SH, LH	Not classified
17009−4154	*Spitzer* SH	PAH
17074−1845	*Spitzer* SL, LL	Sil emission
17088−4221	*Spitzer* SH	Not classified
17130−4029	*Spitzer* SL, SH, LH	PAH
17168−3736	*Spitzer* SH, LH	Sil absorption
17195−2710	*Spitzer* SL, SH, LH	Sil absorption
17203−1534	*Spitzer* SL, LL	Sil emission
17234−4008	*Spitzer* SL, SH, LH	Sil absorption
17253−2831	*Spitzer* SL, LL, SH, LH	Sil absorption
17287−3443	*Spitzer* SL, SH	Transition object with peculiar dust
17311−4924	*Spitzer* SL, LL	Transition object with peculiar dust
17317−2743	*Spitzer* SL, SH, LH	Sil emission
17359−2902	*Spitzer* SL, SH, LH	11-micron source
17364−1238	*Spitzer* SL, LL	Sil emission

Table 1 – *continued*

Object name	Source of spectra	Dust classification
17376−2040	*Spitzer* SL, LL	Not classified
17381−1616	*Spitzer* SL, LL	Sil emission
17423−1755	*Spitzer* SL, LL, *ISO*	featureless
17488−1741	*Spitzer* SL, LL	Not classified
17542−0603	*Spitzer* SL, LL	PAH+Sil
17580−3111	*Spitzer* SL, SH, LH	Not classified
18023−3409	*Spitzer* SL, LL	Sil emission
18062+2410	*Spitzer* SL, LL	Sil emission
18246−1032	*Spitzer* SL, SH, LH	Sil absorption
18533+0523	*Spitzer* SL, SH, LH	PAH
19024+0044	*Spitzer* SL, SH, LH	PAH + sil
19157−0247	*Spitzer* SL, LL, SH, LH	Sil emission
19200+3457	*Spitzer* SL, LL	PAH
19306+1407	*Spitzer* SL, LL, SH	PAH+Sil
19454+2920	*Spitzer* SH	featureless
19477+2401	*Spitzer* SH, LH	Not classified
19590−1249	*Spitzer* SL, LL	Sil emission
20259+4206	*Spitzer* SH, LH	featureless
20462+3416	*Spitzer* SL, LL	PAH+Sil
20572+4919	*Spitzer* SL, LL	Sil emission
21289+5815	*Spitzer* SL, LL	PAH+Sil
21546+4721	*Spitzer* SL, LL	PAH
22023+5249	*Spitzer* SL, LL	PAH+Sil
22036+5306	*Spitzer* SH, LH	Sil absorption
22223+4327	*Spitzer* SL, LL, SH, LH	PAH
F22327−1731	*Spitzer* SL, SH, LH	Sil emission
23304+6147	*Spitzer* SH, LH, *ISO*	PAH

of all programme objects along with their spectral data sources and the type of dust from our classification. Fig. 2(a) gives typical spectra of PAGB candidates, depicting the above classification. The figure shows in the top three panels the raw spectra of the PAGB candidates, on which pivotal points are marked (filled circles; see Spoon et al. 2007) to define the global continuum. The continuum as defined by the pivotal points on the spectra was then fitted by a second- or third-order polynomial for the entire region. In the figure, the continuum-subtracted spectra are shown in the bottom eight panels. The spectra for all individual sources in each class are given in Appendix A. Out of the 71 PAGB sources considered in the present study, 11 objects do not fall under any of the classes. In addition, two PAGB sources showing fine-structure lines have very peculiar dust features that do not fall in the above classification. Among the remaining 58 sources, about 29 per cent of the PAGB sources showed strong or weak/blended PAH features, 26 per cent showed silicate emission, 17 per cent of sources showed PAH along with silicate in emission (mixed chemistry), 12 per cent of sources showed silicate absorption, 11 per cent of sources showed a 11-μm feature and 5 per cent of sources showed featureless spectra.

Some details of the sources in different classes or categories are described below with reference to the spectra beyond 20 μm, up to 38 μm. In this spectral region, the most prominent features seen are at 21 and 30 μm. Among the 17 sources that fall under the PAH category, nine show both 21- and 30-μm features, three sources show only the 30-μm feature and one shows only the 21-μm feature. The sources IRAS 04296+3429, IRAS 05113+1347, IRAS 06530−0213, IRAS 14429−4539, IRAS 15482−5741, IRAS 18533+0523, IRAS 19200+3457, IRAS 22223+4327 and IRAS 23304+6147 show both 21- and 30-μm features. The sources IRAS 01005+7910, IRAS 12145−5834 and IRAS 21546+4721 show only the 30-μm feature, while IRAS 07134+1005 shows only the 21-μm feature. All these sources show strong, blended or weak PAH features also. The presence of 21 μm along with the observed PAH features thus depicts their carbon-rich chemistry.

Silicate emission at both 9.7 and 18 μm were observed in 15 sources. The peak position of silicate emission usually occurs at 9.7 μm, but we found that in some sources the peak occurs at longer wavelengths (≈ 10.1–10.2 μm). Bouwman et al. (2001) suggested an increase in grain size responsible for the change in the 9.7-μm peak position towards longer wavelengths. In the objects that are categorized under this section, a number of sources showed features at 27 and 33 μm attributed to crystalline olivines (see Jaeger et al. 1998). These sources do not show the 21- and 30-μm features. Silicate emission along with PAH (mixed chemistry) has been observed in 10 sources. A number of sources in this category also showed the presence of crystalline olivines at 27 and 33 μm. Waters et al. (1998) proposed a scenario for mixed chemistry in which a presently carbon-rich star may retain circumstellar oxygen-rich gas in its outer layers, due to an earlier phase of mass loss. This scenario can then account for both carbon-rich (PAH emission) and oxygen-rich (silicate emission) signatures. Using SOFIA infrared imager observations combined with 3D photoionization and dust radiative transfer modelling, Guzman-Ramirez et al. (2015) also demonstrated that oxygen-rich (silicate) dust occurs in the outer regions of the planetary nebula BD +30° 3639, while the carbon-rich material (PAHs) is located in the inner parts. These earlier studies suggest the emergence of mixed chemistry, possibly caused by dredge-up of carbon from inner regions of the central star towards the end of the AGB stage.

The absorption due to silicates at 9.7 and 18 μm has been observed in seven sources. The spectral types of all these sources are not known, due to the possibility of their photospheres being heavily enshrouded by circumstellar shells. Garcia & Perea Calderon (2003) suggested an increased thickness of the circumstellar shell responsible for the absorption features in oxygen-rich sources.

The broad 11-μm feature usually attributed to SiC has been observed in IRAS 08005−2356, IRAS 11339−6004, IRAS 14325−6428, IRAS 14341−6211, IRAS 16494−3930 and IRAS 17359−2902. It may be noted that these sources do not show PAH emissions. It is generally believed that SiC emission features are observed in sources with very thick dust shells formed from carbon-based dust grains. Garcia & Perea Calderon (2003) attributed the observed increase in strength of the SiC feature in carbon stars to the increased mass-loss rate during the AGB phase of the stars. Speck, Thompson & Hofmeister (2005) argued that the change in the appearance of the 11-μm feature is a result of self-absorption from thick dust shells. In the longer wavelength region, among the six sources in this category, two sources show the 30-μm feature and two other sources do not show the 30-μm feature but do show crystalline olivines.

Among the three objects that are categorized as showing featureless spectra, the sources IRAS 19454+2920 and IRAS 20259+4206 show a narrow absorption line of the carbon-based molecule C_2H_2 at 13.7 μm, suggesting their advanced stage of evolution towards a carbon-rich star, in addition to the featureless thermal continuum due to dust. On the basis of the observed featureless thermal emission from the circumstellar envelope and a weak Rayleigh–Jeans tail at shorter wavelengths due to the central star, it may be conjectured that objects displaying such spectral characteristics may be relatively young PAGB stars evolving beyond heavily enshrouded OH/IR stars (Waelkens & Waters 2003).

The carrier candidates for the 21- and 30-μm feature are still being debated. Candidates for the 21-μm feature include TiC (von Helden et al. 2000), doped SiC dust (Speck & Hofmeister 2004),

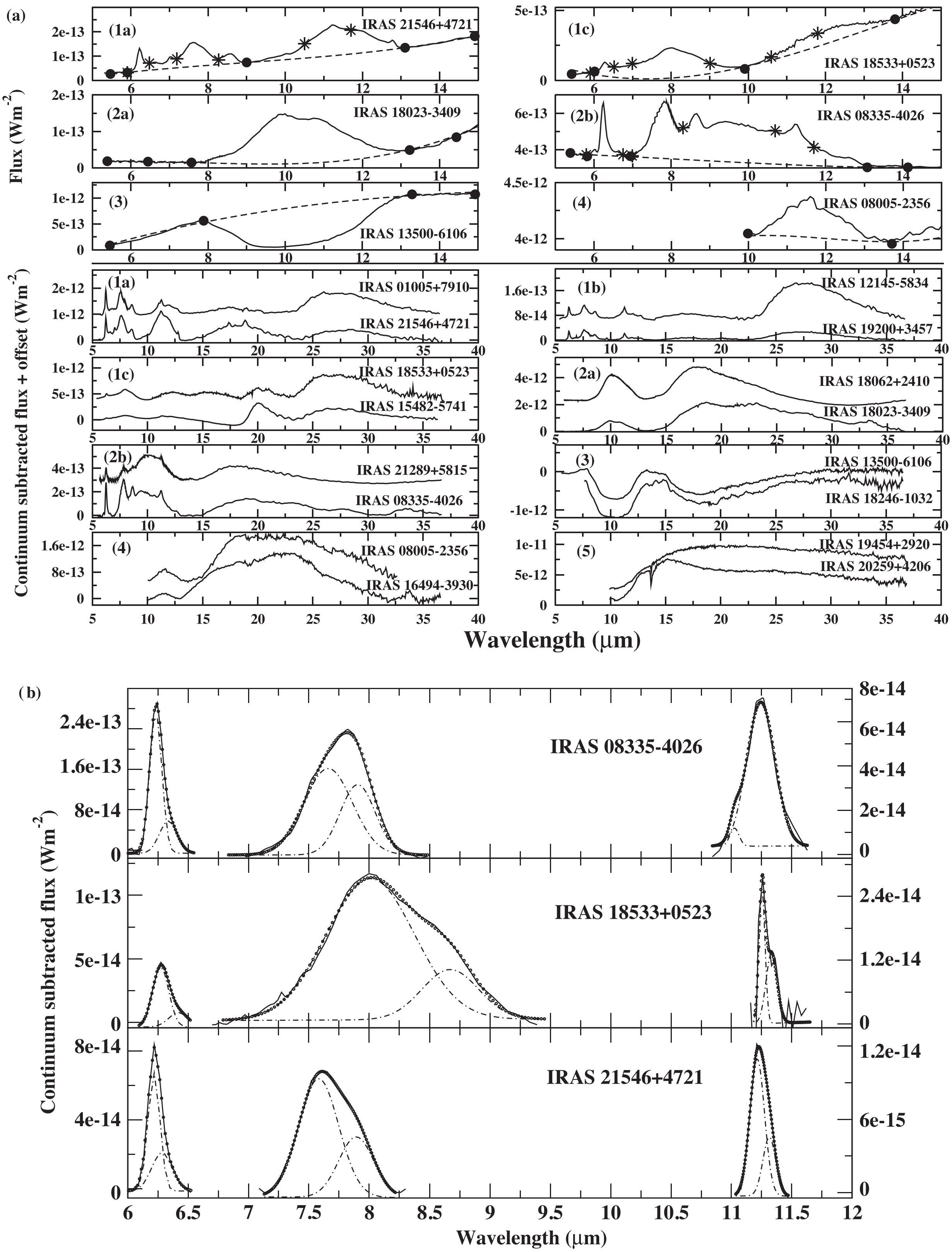

Figure 2. (a) Extracted raw spectra (solid curves) with pivotal points, shown as filled circles, and asterisks for defining the global and plateau continuum in the top three (left and right) panels. Plotted in the bottom eight panels (left and right) are the continuum-subtracted *Spitzer* IRS spectra of the PAGB stars showing (1a) strong PAH features, (1b) weak PAH features (1c) blended PAH feature, (2a) silicate dust emission features, (2b) PAH + silicate emission (mixed chemistry), (3) silicate absorption, (4) the prominent broad bump around 11 μm and (5) featureless spectra (continuum not subtracted). (b) Continuum-subtracted spectra of three sources chosen (from classes 1a, 1c and 2b in Fig. 2a) to illustrate multi-Gaussian decomposition of the main PAH features at 6.2, 7.7 and 11.2 μm. The fitted Gaussian profiles and their sum are represented by dot–dashed and dotted lines, respectively, while the solid curves represent the continuum-subtracted spectra. The flux scale on the right is for the 11.2 μm feature.

Table 2. Equivalent widths (in μm) and peak wavelengths (in μm) of PAH features in the sample PAGB candidates.

Name	Equivalent width			Peak wavelength		
	6.2 μm	7.7 μm	11.2 μm	6.2 μm	7.7 μm	11.2 μm
01005+7910	0.380 ± 0.034	0.379 ± 0.020	0.058 ± 0.005	6.225 ± 0.003	7.555 ± 0.006	11.241 ± 0.003
04296+3429	0.158 ± 0.007	0.183 ± 0.025	0.092 ± 0.008	6.262 ± 0.002	7.829 ± 0.068	11.369 ± 0.013
05113+1347	–	–	0.040 ± 0.005	–	–	11.355 ± 0.004
05341+0852	–	–	0.082 ± 0.006	–	–	11.352 ± 0.003
06530−0213	–	–	0.132 ± 0.027	–	–	11.357 ± 0.007
07134+1005	–	–	0.194 ± 0.017	–	–	11.346 ± 0.004
08335−4026	0.078 ± 0.006	0.108 ± 0.020	0.031 ± 0.006	6.239 ± 0.003	7.703 ± 0.030	11.243 ± 0.002
11353−6037	0.503 ± 0.019	0.514 ± 0.028	0.074 ± 0.005	6.252 ± 0.009	7.773 ± 0.004	11.258 ± 0.003
11387−6113	0.056 ± 0.006	0.050 ± 0.005	–	6.307 ± 0.003	7.893 ± 0.021	–
12145−5834	0.438 ± 0.016	0.368 ± 0.029	0.112 ± 0.009	6.235 ± 0.002	7.597 ± 0.006	11.255 ± 0.007
13313−5838	0.019 ± 0.006	–	–	6.285 ± 0.006	–	–
14429−4539	0.216 ± 0.030	0.356 ± 0.023	0.100 ± 0.019	6.267 ± 0.006	7.938 ± 0.007	11.311 ± 0.006
14482−5725	0.041 ± 0.008	0.105 ± 0.020	0.048 ± 0.006	6.298 ± 0.003	8.164 ± 0.012	11.238 ± 0.011
15482−5741	0.114 ± 0.025	0.266 ± 0.022	0.048 ± 0.005	6.262 ± 0.010	7.968 ± 0.009	11.297 ± 0.009
17009−4154	–	–	0.049 ± 0.006	–	–	11.253 ± 0.003
17130−4029	0.051 ± 0.007	0.174 ± 0.014	–	6.275 ± 0.009	8.065 ± 0.013	–
17542−0603	0.011 ± 0.007	0.013 ± 0.005	0.057 ± 0.006	6.312 ± 0.002	7.899 ± 0.002	11.305 ± 0.011
18533+0523	0.072 ± 0.009	0.562 ± 0.007	0.011 ± 0.004	6.282 ± 0.002	7.991 ± 0.004	11.260 ± 0.011
19024+0044	0.090 ± 0.004	0.021 ± 0.004	–	6.265 ± 0.002	7.740 ± 0.006	–
19200+3457	0.441 ± 0.009	0.241 ± 0.041	0.212 ± 0.040	6.232 ± 0.002	7.590 ± 0.014	11.268 ± 0.004
19306+1407	0.339 ± 0.005	0.251 ± 0.021	0.006 ± 0.003	6.239 ± 0.007	7.820 ± 0.008	11.242 ± 0.011
20462+3416	0.215 ± 0.025	0.343 ± 0.007	0.012 ± 0.064	6.233 ± 0.007	7.692 ± 0.018	11.254 ± 0.018
21289+5815	0.100 ± 0.029	0.069 ± 0.005	0.016 ± 0.005	6.241 ± 0.007	7.832 ± 0.017	11.238 ± 0.014
21546+4721	0.170 ± 0.009	0.117 ± 0.034	0.007 ± 0.002	6.226 ± 0.002	7.592 ± 0.014	11.226 ± 0.002
22023+5249	0.304 ± 0.038	0.373 ± 0.058	0.025 ± 0.005	6.220 ± 0.002	7.743 ± 0.009	11.218 ± 0.006
22223+4327	0.025 ± 0.004	0.099 ± 0.009	0.032 ± 0.006	6.267 ± 0.004	7.880 ± 0.028	11.287 ± 0.004
23304+6147	–	–	0.089 ± 0.004	–	–	11.360 ± 0.008

FeO (Posch, Mutschke & Andersen 2004) and PAH molecules (Justtanont et al. 1996). Goebel & Moseley (1985) suggested solid magnesium sulphide (MgS) as the possible carrier for the 30-μm feature, while Duley (2000) suggested carbon-based linear molecules with specific side groups.

For the purpose of analysing the correlations, equivalent widths (EWs) of the most prominent mid-infrared PAH features, namely those at 6.2, 7.7 and 11.2 μm, were derived using the Spectroscopic Modelling Analysis and Reduction Tool (SMART). Table 2 lists the EWs for all objects that showed PAH features. The table also lists the peak positions of the three features for each object. EWs of the three PAH features considered here were determined using the procedures adopted by Hony et al. (2001), Peeters et al. (2002) and Peeters et al. (2017). In addition to the global continuum as shown in Fig. 2(a), the local continuum around the 5–12 μm region is enhanced by broad plateaus around 5–7 μm, 7–8 μm (8-μm bump) and 10–12 μm (see Peeters et al. 2017, and the references therein). These plateaus are typically shown by asterisks in Fig. 2(a) (see class 1a, 1c, 2b in the top three panels). The pivotal points defining the plateau continua were fitted by second- or third-order polynomials and subtracted from the raw spectra. The resulting continuum-subtracted spectra around 6.2, 7.7 and 11.2 μm were fitted suitably by single/multi Gaussian profiles (using the LINE FIT task in SMART) to account for the PAH emission features. In most cases, spectral decomposition using two Gaussians was required to account for blended components of PAH emission in 7- and 11-μm regions, while the 6.2-μm feature required a single Gaussian in six objects, two in 12 and three Gaussians in three objects. Fig. 2(b) shows continuum-subtracted spectra of three objects (classes 1a, 1c and 2b) for which Gaussian decomposition is illustrated. In the literature, several methods have been used to extract the intensity or EWs of PAH features (e.g. Drude profiles (Smith et al. 2007), Lorentzian (Galliano et al. 2008) and Gaussian (Uchida et al. 2000; Hony et al. 2001; Peeters et al. 2002, 2017; Blasberger et al. 2017)). In a recent study, Peeters et al. (2017) concluded that for a large sample of objects PAH correlations are independent of the method adopted. The earlier studies suggested that the line fluxes were only marginally affected by the choice of profile, depending more on the choice of continuum. Further, the line-centre determination does not depend critically upon the choice of profile (e.g. Blasberger et al. 2017). The errors in the EW of the PAH features (see Table 2) were estimated using the relation

$$\sigma_{\mathrm{T}}^2(W) = M.\left(\frac{h_\lambda}{S/N}\right)^2.\frac{\tilde{F}_j}{\tilde{F}_{\mathrm{c}}} + \left[\frac{\sigma(\tilde{F}_{\mathrm{c}})}{\tilde{F}_{\mathrm{c}}}.(\Delta\lambda - W)\right]^2 \quad (1)$$

from Chalabaev & Maillard (1983), where h_λ is the spectral resolution per pixel, M the number of pixels, S/N the signal-to-noise ratio, $\tilde{F}_j/\tilde{F}_{\mathrm{c}}$ represents the ratio of measured flux over the continuum summed over the number of pixels, $\sigma(\tilde{F}_{\mathrm{c}})$ represents the uncertainty in the continuum, $\Delta\lambda = \lambda_1 - \lambda_2$ is the wavelength range covered by the feature and W represents the EW.

4 MODELLING OF SEDS

The SEDs of the sample stars constructed from archival photometric data were modelled using the software DUSTY (Ivezic, Nenkova & Elitzur 1999). The input parameters for each object consist of stellar photospheric temperature (T_*), temperature of the inner region of the dust shell (T_{d}), composition of the dust grains, density distribution and the optical depth at 0.55 μm ($\tau_{0.55}$). The composition of the dust considered here for the individual sources is based on the observed spectral features in their *Spitzer* IRS spectra. The parameters that are fixed are T_*, dust particle size limits, size distribution index and density distribution. The variable parameters are T_{d}, composition of dust grains (for continuum we mainly used either graphite (Gr) or amorphous carbon (AmC)) and optical depth at 0.55 μm ($\tau_{0.55}$). The code solves the radiative transfer problem for a source embedded in a spherically symmetric dusty envelope. The important output parameters of the code are the total flux as a function of wavelength, the inner shell radius r_1, the ratio of the inner shell radius and the radius of the central source r_1/r_c, the terminal velocity and the upper limit of the mass of the source. The model also gives an estimate of the total mass-loss rate ($\mathrm{d}M_{\mathrm{gas+dust}}/\mathrm{d}t = \dot{M}$) for envelope expansion caused by radiatively driven winds with an uncertainity of 30 per cent. Meixner et al. (1997) and Mishra et al. (2016) used axisymmetric models to infer mass-loss rates. We find a good agreement with these models for some sources that are common in our sample.

The model fluxes are compared with the observed values by normalizing with the flux at either the 2-μm (K) or 9-μm band (of MSX or *AKARI* or IRAC) depending upon the distribution of observed data points in the infrared range. T_* was taken from Allen (2000) and Lang (2006) for objects with spectral types that are identified. For all the other objects (25 in number) for which spectral types are unavailable, we have estimated T_* from model best fits. For the majority of programme objects, the best-fitting degeneracy is very minimal and can be gauged by the uncertainty in $T_{\rm d}$ (<5 per cent) and $\tau_{0.55}$ (about 10 per cent), the grain composition that contributes for the continuum (< 10 per cent). The criterion for the best fit was chosen as $\chi^2 = \Sigma_i[(F_{\mathrm{O}i} - F_{\mathrm{M}i})^2/F_{\mathrm{M}i}] \le 10^{-12}$, where Σ_i indicates summing over all data points ($i = 1$ to n, n being the number of data points for a particular source) and $F_{\mathrm{O}i}$ and $F_{\mathrm{M}i}$ are the observed and model fluxes at the ith data point, respectively. For each object, several models were generated by tweaking the variable parameters ($T_{\rm d}$, grain composition and $\tau_{0.55}$) and we chose the best model as determined by the chi-square criterion as well as by visual inspection. Barring a few cases, for most sources in our sample the limit on χ^2 resulted in (visually) reasonably good fits. It may be noted that the spectral class differences in some of the objects that are common to SIMBAD and Suarez et al. (2006) did not alter the model-derived parameters by more than 10 per cent.

In general, the double-humped SEDs of PAGB stars indicate detached dust shells, in contrast with AGB stars (Venkata Raman & Anandarao 2008). For the purpose of modelling, we have divided our sample stars into two categories, based on their IRS spectra: (i) those that show clearly the PAH features in the 6–15 μm region and (ii) those showing no PAH features at all. Strong and weak/blended PAHs were modelled using a double-shell geometry, because PAH alone could not account for the continuum emission on either side of the 5–15 μm region, while the sources with silicate in emission/absorption and broad 11-μm feature were modelled using single-shell geometry. A SED model using a single dust shell with graphite, amorphous carbon, SiC and silicate dust grains or a combination of these, as the case may be, represented circumstellar sources without PAH emission better. SED models using two shells better modelled strong, weak/blended PAH and mixed chemistry sources, with an inner shell of PAH and an outer shell containing graphite or amorphous carbon or silicate dust grains. The optical constants for the PAH were provided externally into DUSTY, while the other dust grains used here are inbuilt with DUSTY. A modified Mathis-Rumpl-Nordsieck (Mathis, Rumpl & Nordsieck 1977) dust-size distribution was assumed with an exponent of 3.5, with minimum and maximum dust grain sizes of 0.005 and 0.25 μm, respectively. A radiatively driven wind model was chosen for the dust shell, with density distribution of type 3 (see Ivezic & Elitzur 1995), in which the envelope expansion is owing to the radiation pressure on dust-grain particles (see Ivezic & Elitzur 1997). Table 3 shows the list of single-shelled PAGB sources along with model-derived photospheric and circumstellar shell parameters, namely T_*, $T_{\rm d}$, $\dot{M}$, $\tau_{0.55}$, r_1, r_1/r_c and the grain composition (Gr is for graphite, AmC for amorphous carbon and Sil for silicate grains, with the portion in 1 given in parentheses). Also listed in Table 3 are the dust mass-loss rates $\dot{M}_{\rm d}$, using the following empirical relation by Lagadec et al. (2008):

$$\log(\dot{M}_{\rm d}) = -9.58 + 0.26(K_{\rm s} - [11]) + 0.05(K_{\rm s} - [11])^2 - 0.0053(K_{\rm s} - [11])^3, \tag{2}$$

where $K_{\rm s}$ and [11] are the magnitudes of the sources in the 2MASS K band and VISIR PAH2 filter ($\lambda_{\rm c}$= 11.25 μm, $\Delta\lambda$=0.59 μm), respectively. The dust mass-loss rates obtained from infrared colours were found to be in the range between 10^{-8} and 10^{-10} $\mathrm{M}_{\odot}$ yr^{-1}, agreeing well with the results of Lagadec et al. (2008). It is clear from the table that the grain composition for all sample stars is carbonaceous dust (either graphite or amorphous carbon or a combination of the two). This result, however, does not fall in line with the finding of Cerrigone et al. (2009), whose sample showed only 25 per cent having carbon-rich envelopes. Fig. 3 shows typical model fits for PAGB stars with single shells. Photometric observations as well as *Spitzer* IRS spectra are overplotted for comparison.

For those sources (27 in number) in which the *Spitzer* IRS spectra showed strong PAH emission, we have used two spherical shells (instead of one used before) for the SED modelling using DUSTY. The first or inner shell contains predominantly neutral or ionized PAH and the second, outer shell contains any of the common dust grains (amorphous carbon/silicate/graphite). The ratio of the 6.2- or 7.6-μm PAH over 11.2-μm feature can be used as a measure of the ionization fraction of PAHs, because the ionized PAHs emit more strongly in the 6.2- and 7.6-μm bands, while the 11.2-μm band is stronger in neutral PAHs. This ratio may be estimated from *Spitzer* mid-IR spectra and whether the PAHs are neutral or ionized may be ascertained in a given source. The optical properties obtained from Draine & Li (2001) for neutral and ionized PAHs with a grain size of 0.01 μm were used as external input to the DUSTY software. A density distribution falling off as r^{-2} was used for both dust shells. Fig. 4 shows typical model fits with double shells for the PAGB candidates. Table 4 show the list of these PAGB sources along with the derived photospheric and circumstellar shell parameters, T_*, $T_{\rm d}$, ionized state of PAH in the first sphere, r_1, r_1/r_c for both the shells and the grain composition in dust shell 2. It is assumed that PAH and dust exist in two separate shells, with the former closer to the star than the latter. The PAH emission may be from regions very close to the edge of the photodissociation regions.

We note here that it may be quite reasonable to assume that PAH molecules exist in a separate shell closer to the star, because they require soft UV radiation for excitation. Further, it is possible that the PAH shell could form close to the central star during the most recent PAGB mass-loss episode, where the outer layer of the central star is enriched with carbon-rich materials due to a thermal pulse. As mentioned earlier, Waters et al. (1998) used similar arguments for explaining the observed the oxygen- and carbon-rich signatures in the binary system of the Red Rectangle. Also, Guzman-Ramirez et al. (2015) suggested that, in the planetary nebula BD +30° 3639, carbonaceous dust (PAH) exists in the inner regions while oxygen-rich dust (silicates) exists in the outer regions of the nebula.

Table 3. Parameters derived from SED modelling of PAGB candidates using DUSTY; the spectral types are from SIMBAD and Suarez et al. (2006) and both the total and dust mass-loss rates are in units of $M_{\odot}$ yr^{-1}.

Object	Sp. type	T_*	T_d	$\tau_{0.55}$	Grain type	r_1 (m)	r_1/r_c	$\dot{M}$	$\dot{M}_d$
05089+0459	M3I	3500	200	6.0	AmC(1.0)	2.1E+14	1.1E+03	5.8E−05	4.4E−09
06034+1354	–	5000	300	1.5	AmC(0.9)+Sil(0.1)	7.6E+13	8.2E+02	1.9E−05	2.2E−09
06556+1623	Bpe	15000	240	0.3	AmC(0.6)+Gr(0.4)	2.1E+14	2.1E+04	1.5E−05	6.1E−10
08005−2356	F5e	6650	440	5.0	Gr(0.9)+SiC(0.1)	5.4E+13	1.0E+03	3.1E−05	8.1E−10
10211−5922	–	5000	250	0.3	Gr(0.9)+Sil(0.1)	1.1E+14	1.2E+03	7.5E−06	1.4E−10
11201−6545	A3Ie	6000	150	5.0	Sil(0.5)+AmC(0.5)	3.5E+14	5.5E+03	8.7E−05	2.0E−09
11339−6004	–	14000	190	8.0	AmC(0.9)+SiC(0.1)	4.0E+14	3.4E+04	1.0E−04	7.6E−08
13245−5036	A7Ie	7650	200	7.0	AmC(1.0)	2.9E+14	7.5E+04	8.2E−05	1.5E−10
13500−6106	–	11000	280	20.0	AmC(0.1)+Gr(0.1)+Sil(0.8)	8.2E+13	4.2E+03	1.0E−04	2.9E−08
13529−5934	–	12000	200	13.0	AmC(0.2)+Gr(0.8)	3.6E+14	2.2E+04	1.2E−04	1.8E−08
14325−6428	F5I	6640	160	2.5	AmC(0.9)+SiC(0.1)	5.0E+14	9.6E+03	6.6E−05	1.6E−09
14341−6211	–	6000	195	10.0	AmC(0.9)+SiC(0.1)	2.9E+14	4.5E+03	9.5E−05	1.9E−08
14346−5952	–	12000	500	10.0	Gr(0.9)+AmC(0.1)	5.0E+13	3.1E+03	4.0E−05	5.5E−10
16206−5956	A3Iab:e	8000	105	0.7	AmC(0.3)+Sil(0.7)	7.6E+14	2.1E+04	5.1E−05	1.9E−10
16494−3930	G2I	5160	200	8.0	AmC(0.8)+Gr(0.1)+SiC(0.1)	2.5E+14	2.9E+03	7.9E−05	8.2E−08
16559−2957	F5Iab:e	6650	220	4.0	AmC(0.7)+Sil(0.3)	1.6E+14	3.1E+03	5.1E−05	1.0E−08
17074−1845	B5Ibe	11000	140	3.0	Sil(1.0)	3.3E+14	1.7E+04	1.0E−04	2.1E−09
17088−4221	–	14000	250	15.0	AmC(0.1)+Gr(0.9)	2.4E+14	2.1E+04	1.0E−04	6.1E−08
17168−3736	–	14000	190	12.0	Gr(0.9)+Sil(0.1)	3.9E+14	3.3E+04	1.2E−04	9.4E−08
17195−2710	–	8000	370	9.0	Gr(0.9)+Sil(0.1)	8.1E+13	2.2E+03	5.0E−05	2.6E−09
17203−1534	B1IIIpe	10000	130	2.5	Gr(0.3)+Sil(0.7)	5.0E+14	2.1E+04	9.0E−05	1.4E−09
17234−4008	–	14000	175	10.0	Gr(0.9)+Sil(0.1)	4.6E+14	3.9E+04	1.2E−04	1.7E−08
17253−2831	–	5000	150	4.0	AmC(0.7)+Gr(0.2)+Sil(0.1)	4.5E+14	4.9E+03	7.6E−05	1.3E−09
17287−3443	–	18000	150	20.0	AmC(0.3)+Gr(0.7)	7.4E+14	1.0E+05	2.0E−04	1.9E−08
17311−4924	B1Iae	15000	200	3.0	Gr(0.4)+Sil(0.6)	2.3E+14	2.9E+04	6.7E−05	2.4E−10
17317−2743	F5I	6640	140	7.5	Gr(0.9)+Sil(0.1)	5.2E+14	9.9E+03	1.1E−04	4.1E−10
17359−2902	–	8000	230	15.0	Gr(0.9)+SiC(0.1)	2.4E+14	6.6E+03	1.0E−04	5.3E−09
17364−1238	–	8000	130	1.0	AmC(0.1)+Sil(0.9)	3.2E+14	8.9E+03	4.6E−05	3.4E−10
17376−2040	F6I	6460	280	4.0	AmC(0.5)+Gr(0.5)	1.2E+14	2.2E+03	4.1E−05	9.1E−10
17381−1616	B1Ibe	20700	400	1.0	AmC(0.9)+Sil(0.1)	5.7E+13	1.0E+04	1.7E−05	5.1E−09
17423−1755	Be	13000	170	5.0	Gr(0.8)+Sil(0.2)	4.0E+14	2.6E+04	8.6E−05	7.7E−10
17488−1741	F7I	6280	260	6.5	Gr(1.0)	1.6E+14	2.8E+03	6.0E−05	1.6E−10
17580−3111	–	5000	290	15.0	Gr(1.0)	1.1E+14	1.2E+03	7.3E−05	1.2E−08
18023−3409	B2IIIe	10000	175	1.0	AmC(0.3)+Sil(0.7)	2.2E+14	9.6E+03	3.7E−05	3.0E−09
18062+2410	B1IIIpe	18000	200	1.0	Sil(1.0)	1.9E+14	2.6E+04	4.5E−05	4.0E−08
18246−1032	–	20000	130	20.0	Gr(0.8)+Sil(0.2)	8.5E+14	1.3E+05	2.2E−04	2.6E−08
19157−0247	B1III	15000	800	2.0	Gr(0.8)+Sil(0.2)	1.5E+13	1.5E+03	1.2E−05	1.5E−09
19454+2920	–	10000	180	7.0	AmC(1.0)	4.2E+14	1.8E+04	9.7E−05	4.1E−08
19477+2401	F4I	6820	200	10.0	AmC(0.8)+Gr(0.2)	2.8E+14	5.7E+03	9.7E−05	2.7E−10
19590−1249	B1Ibe	20000	125	0.1	Gr(0.3)+Sil(0.7)	7.1E+14	1.2E+05	1.8E−05	1.0E−09
20259+4206	F3I	6990	200	8.0	AmC(1.0)	2.9E+14	6.1E+03	8.5E−05	2.3E−08
20572+4919	F3Ie	7700	265	2.0	Gr(0.85)+Sil(0.15)	1.2E+14	2.9E+03	2.9E−05	8.3E−10
22036+5306	–	8000	140	8.0	AmC(0.7)+Gr(0.2)+Sil(0.1)	6.7E+14	1.8E+04	1.3E−04	1.3E−09
F22327−1731	A0III	7600	600	0.35	Gr(0.85)+Sil(0.15)	2.2E+13	5.5E+02	4.6E−06	7.5E−10

5 RESULTS AND DISCUSSION

5.1 Dust-formation distance

The SED modelling reveals a few interesting, physically viable relationships between various derived parameters. Fig. 5 shows a plot of the inner dust temperature and inner radius of the dust shell for all the stars in our sample. In the case of objects showing PAH spectra, the inner radii of both the PAH and dust shells are shown in the figure. The plot shows that, as the dust temperature increases, the radius of the inner shell decreases. This simply implies that the dust gets cooler as it is located farther from the star. It may be inferred from the figure that the inner radius of the dust shell corresponding to a typical condensation temperature for (silicate) dust grains, $T_c \sim 1600$ K, is $\sim 3.5 \times 10^{12}$ m. This indicates that the dust-formation distance from the stellar photosphere is typically a few stellar radii. It was argued by Woitke, Goeres & Sedlmayr (1996) and Sedlmayr & Winters (2000) that, for pulsationally driven mass loss to be most efficient, dust formation should occur at a few stellar radii (R_*).

Fig. 6 shows a plot of T_* as a function of ratio r_1/r_c. The plot indicates that the ratio increases with T_*. As the photospheric temperature increases, the star emits a copious amount of UV photons that destroy the dust and hence the dust can survive only at distances far from the star. This explains the positive correlation between the two parameters. This is in line with the above argument on the minimum distance of dust formation.

5.2 Trends in the mass-loss rates

The PAGB mass loss mechanisms are not well-understood and are still being debated. Initially, a continued or extended superwind

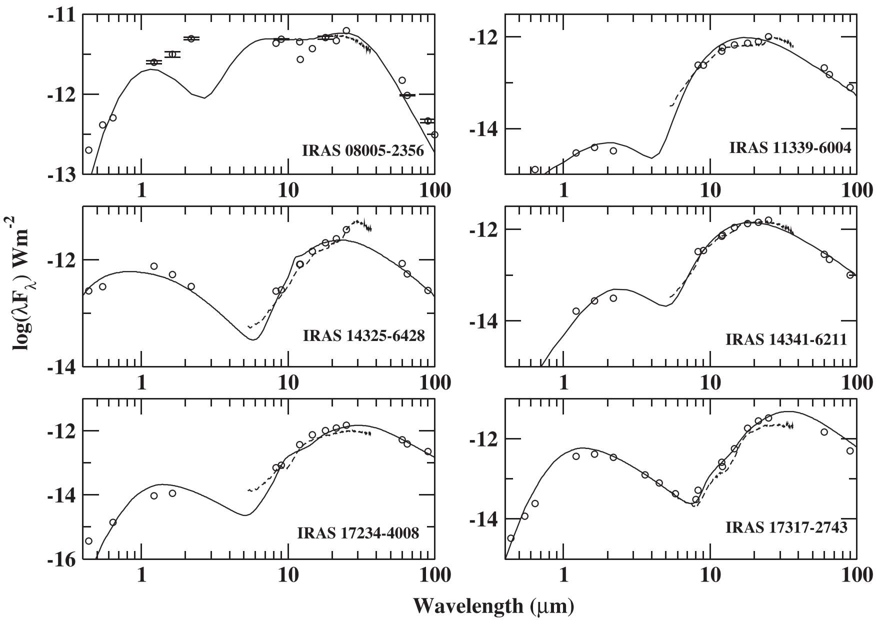

Figure 3. Model SEDs with single spherical shells using DUSTY (solid line) for a few PAGB sources compared with observed data from the literature (open circles). The *Spitzer* IRS spectra (dashed line) are shown for comparison. Being on a log scale, the error bars are of point size.

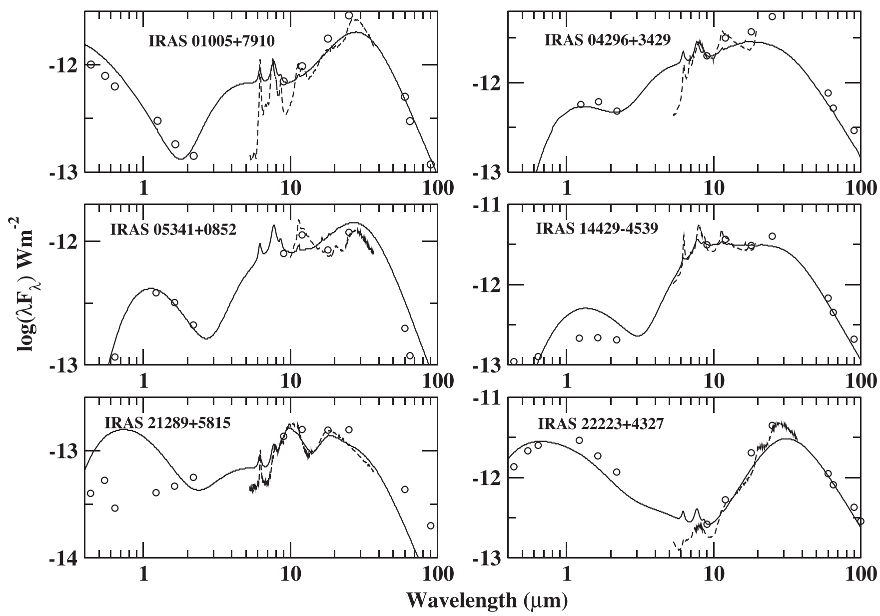

Figure 4. Model SEDs with two spherical shells using DUSTY (solid line) for a few PAGB sources that showed strong PAH emission compared with observed data from the literature (open circles). The *Spitzer* IRS spectra (dashed line) are shown for comparison. Being on a log scale, the error bars are of point size.

phase until the central star attains a certain temperature was assumed in order to explain the PAGB mass-loss rates (Schoenberner 1983). However, very recently Hrivnak, Lu & Nault (2015) attributed the variation in the PAGB light curve to pulsations that levitate the circumstellar envelopes to sufficient heights, leading to dust formation. As the central stars evolve and the temperature increases, radiation-driven winds facilitate the mass-loss process (Vassiliadis & Wood 1994). The mass-loss rates obtained from the model for our sample of PAGB stars showed the expected trends with the other model-derived parameters. Despite considerable scatter, especially for optically thin cases ($\tau_{0.55} \leq 1.0$), one may infer from Fig. 7 an increasing trend in mass-loss rate with optical depth at 0.55 μm. During the mass-loss process, the dust shell initially remains optically thin, allowing radiation from the central star to escape. However, as the mass loss increases, the optical depth increases, leading to the formation of a thick circumstellar shell resulting in the formation of dust that completely blocks the radiation escaping the central star. These are physically expected results and hence the plots serve as a validation of circumstellar dust shell properties. Fig. 8 shows the tendency of decreasing mass-loss rate with increasing inner dust temperature, in line with the above arguments. Since most of the dust grains (silicates and graphites) condense at approximately at the same temperature around 1500 K (Salpeter 1977), a strong dependence on the effective temperature (T_*) is expected. An increase in the stellar temperature moves the dust nucleation region outward and hence towards lower densities, which leads to an ineffective

Table 4. Parameters derived with two shells in the SED modelling using DUSTY for the PAGB candidates; the spectral types are from SIMBAD and the total mass-loss rates are in units of $M_{\odot}$ yr^{-1}.

Objects	Sp. type	T_*	Sphere 1					Sphere 2			$\dot{M}$
			PAH type	T_d	r_1 (m)	r_1/r_c	Grain type	T_d	r_1 (m)	r_1/r_c	
01005+7910	B2Iab:e	15000	ionized	700	3.1E+13	3.0E+03	Gr(1.0)	250	2.5E+14	2.4E+04	4.0E−05
04296+3429	G0Ia	5510	ionized	600	1.9E+13	2.5E+02	AmC(0.9)+Gr(0.1)	200	2.6E+14	3.4E+03	6.6E−05
05113+1347	G8Ia	4900	neutral	250	1.5E+14	1.6E+03	AmC(1.0)	200	2.4E+14	2.5E+03	4.7E−05
05341+0852	F4Iab	6820	neutral	500	4.2E+13	8.4E+02	Gr(1.0)	350	9.6E+13	1.9E+03	3.4E−05
06530−0213	F0Iab:	7300	neutral	250	2.4E+14	5.6E+03	Gr(1.0)	100	1.2E+15	2.8E+04	5.0E−05
07134+1005	F5Iab:	6650	neutral	600	2.5E+13	4.7E+02	AmC(1.0)	150	6.1E+14	1.1E+04	3.4E−05
08335−4026	B8e	11500	ionized	700	2.7E+13	1.5E+03	Gr(0.95)+Sil(0.05)	100	1.3E+15	7.9E+04	1.2E−05
11353−6037	B5Ie	13400	ionized	500	7.3E+13	5.6E+03	Gr(1.0)	220	3.0E+14	2.3E+04	6.4E−05
11387−6113	A3I	8890	neutral	190	5.4E+14	1.85E+04	Gr(0.8)+Sil(0.2)	150	4.7E+14	1.6E+04	7.2E−05
12145−5834	–	10000	ionized	500	5.9E+13	2.5E+03	Gr(1.0)	100	1.3E+15	5.7E+04	7.4E−05
13313−5838	K1III	4600	neutral	400	4.8E+13	4.4E+02	Gr(0.2)+AmC(0.8)	200	2.3E+14	2.1E+03	3.1E−05
14429−4539	F4I	6820	ionized	400	7.0E+13	1.4E+03	Gr(0.6)+AmC(0.4)	320	9.7E+13	1.9E+03	4.1E−05
14482−5725	A2I	9080	neutral	400	4.2E+13	2.9E+02	Gr(1.0)	300	9.1E+13	6.2E+02	3.6E−05
15482−5741	F7I	6100	ionized	400	6.1E+13	9.9E+02	AmC(1.0)	150	5.9E+14	9.4E+03	8.3E−05
17009−4154	–	4500	neutral	250	1.4E+14	1.2E+03	Gr(1.0)	100	8.9E+14	7.8E+03	8.7E−05
17130−4029	–	14000	ionized	1300	5.7E+12	4.8E+02	Gr(0.2)+AmC(0.8)	120	1.2E+15	1.0E+05	6.5E−05
17542−0603	Ge	5500	ionized	1000	5.0E+12	6.5E+01	Gr(1.0)	500	3.7E+13	4.8E+02	1.6E−05
18533+0523	–	5000	ionized	400	5.0E+13	5.4E+02	Gr(0.7)+AmC(0.3)	100	1.0E+15	1.1E+04	9.4E−05
19024+0044	–	10000	ionized	1200	5.6E+12	2.4E+02	AmC(0.8)+Sil(0.2)	130	8.4E+14	3.6E+04	1.1E−04
19200+3457	B...	12000	ionized	500	6.7E+13	4.1E+03	Gr(1.0)	230	2.5E+14	1.5E+04	1.5E−05
19306+1407	B0:e	15400	ionized	800	2.2E+13	2.3E+03	Gr(1.0)	100	1.6E+15	1.6E+05	8.9E−05
20462+3416	B1Iae	20800	ionized	150	1.5E+15	2.9E+05	Gr(0.5)+AmC(0.5)	100	1.7E+15	3.3E+05	1.7E−05
21289+5815	A2Ie	7000	ionized	700	1.7E+13	3.5E+02	Gr(0.7)+Sil(0.3)	300	8.6E+13	1.8E+03	3.9E−05
21546+4721	–	10000	ionized	500	5.9E+13	2.5E+03	Gr(1.0)	200	3.4E+14	1.4E+04	4.3E−05
22023+5249	Be	12000	ionized	200	6.1E+14	3.8E+04	Gr(0.2)+AmC(0.8)	160	5.9E+14	3.6E+04	8.7E−05
22223+4327	F9Ia	6100	ionized	700	1.4E+13	2.3E+02	Gr(1.0)	180	3.2E+14	5.2E+03	3.7E−05
23304+6147	G2Ia	5200	neutral	400	5.5E+13	6.4E+02	Gr(0.5)+AmC(0.5)	170	3.6E+14	4.1E+03	4.3E−05

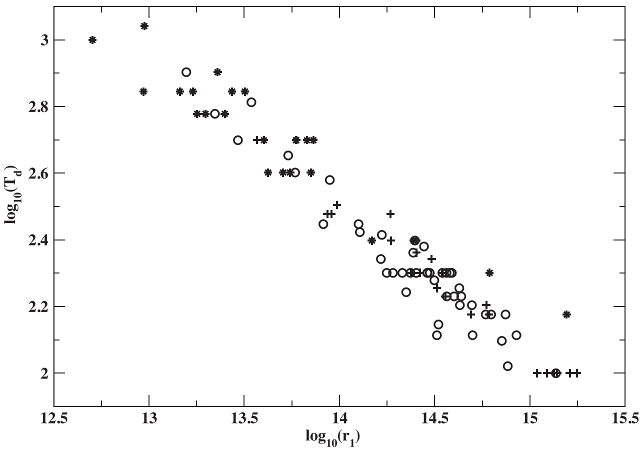

Figure 5. Plot of dust temperature $T_{\rm d}$ versus the inner dust shell radius r_1 (in m) for PAGB stars (open circles) obtained from DUSTY SED models with a single shell irradiated by radiatively driven winds. The asterisk and pluses represent sphere 1 (PAH) and sphere 2 for PAGB candidates modelled with a double circumstellar shell geometry.

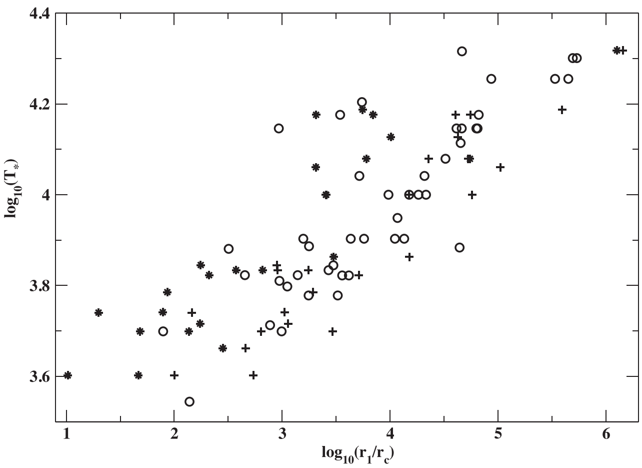

Figure 6. Plot of central source temperature T_* versus the ratio of the inner dust shell radius r_1 and the central source radius $r_{\rm c}$ for PAGB stars (open circles) obtained from DUSTY SED models with a single shell irradiated by radiatively driven winds. The asterisks and pluses represent sphere 1 (PAH) and sphere 2 for PAGB candidates modelled with a double shell geometry.

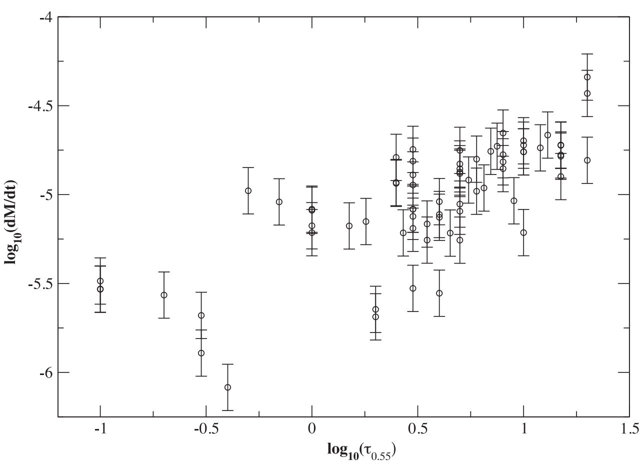

Figure 7. Plot of total mass-loss rate dM/dt versus optical depth at 0.55 μm $\tau_{0.55}$ for PAGB stars.

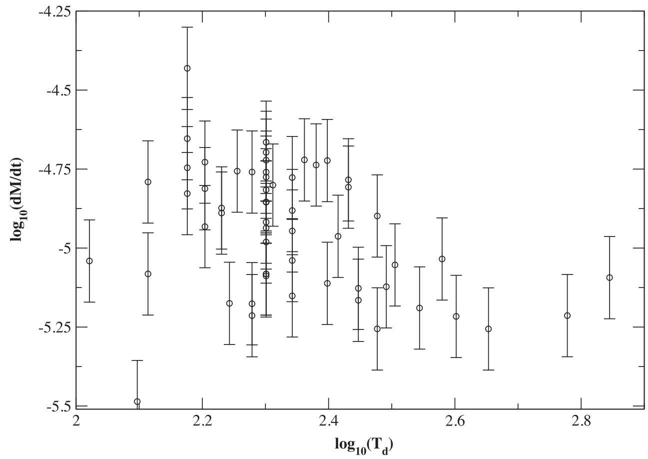

Figure 8. Plot of total mass-loss rate dM/dt versus dust temperature $T_{\rm d}$ for PAGB stars.

coupling between gas and dust, thereby decreasing the mass-loss rates (Lamers & Cassinelli 1999). Also, as $T_{\rm d}$ increases the dust shells tend to be located closer to the central star where dust is destroyed, leading to a low mass-loss rate.

The colour $[K - 12]$ is often considered as an indicator of mass loss in AGB/PAGB stars (Le Bertre & Winters 1998). Anandarao, Pottasch & Vaidya (1993) proposed that the colour index $[25 - 2]$ is a better tool for representing the mass-loss rate in AGB stars. Fig. 9 shows a plot of total mass-loss rates for all those PAGB stars that have single dust shells with $[25 - 2]$ and $[K - 12]$. Also included in the figure are the sample of AGB stars from our previous work (Venkata Raman & Anandarao 2008). The figure indicates that the mass-loss rate does not cease completely towards the end of the AGB phase, but extends beyond and towards the PAGB phase. The PAGB mass-loss rate was found to be much higher than that during the AGB phase. Fig. 9 also shows the mass-loss rates for some PAGB stars (common with our sample) determined from the observed CO rotational line profiles by several authors, namely Woodsworth, Kwok & Chen (1990), Likkel et al. (1991), Omont et al. (1993), Hrivnak & Kwok (1999), Bujarrabal et al. (2001), Hoogzaad et al. (2002) and Hrivnak & Bieging (2005). One can see a good agreement between the model values and those determined by observations. Fig. 10 shows a plot of dust mass-loss rates as a function of the colours $[25 - 2]$ and $[K - 12]$, indicating a similar trend to the total mass-loss rate. Fig. 9 shows two distinct regions: an initial positive correlation of mass-loss rate with $[K - 12]$ and $[25 - 2]$ colours due to the initiation of a superwind towards the end of the AGB phase and continued constant high mass-loss rates during the PAGB stage, possibly due to pulsation and radiatively driven winds from the central star. Recently, de Vries et al. (2014) suggested intense mass loss due to 'hyperwinds' that occur between the superwind and the PPN phase to explain the high mass-loss rates during the PAGB phase. It is, however, not clear as to what causes such a hyperwind, or for that matter the superwind itself. de Vries et al. (2015) also suggested the presence of crystalline forsterite (Mg_2SiO_4) as a signature for massive AGB stars. Based on the variation in the circumstellar nebular conditions and the observed variations in the spectral features, Garcia & Perea Calderon (2003) had proposed an evolutionary scheme for both oxygen- and carbon-rich sources in transition from the AGB to the PN phase. About 15 stars in our sample show the presence of crystalline forsterite at the 33.6-μm feature, possibly suggesting their massive nature. These massive AGB stars cannot lose their entire envelope during

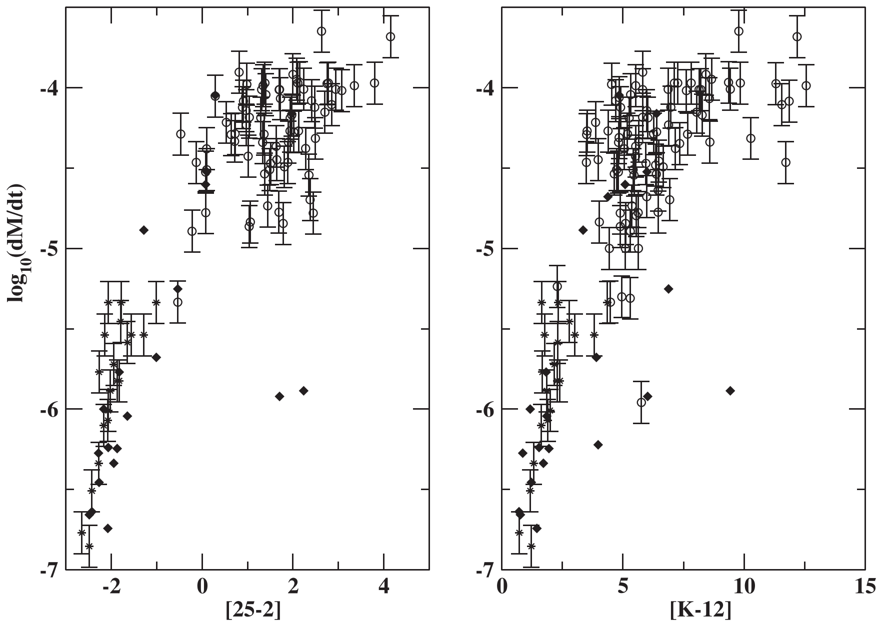

Figure 9. Plot of the total mass-loss rate obtained from DUSTY with mass-loss indexes $[25-2]$ and $[K-12]$ for AGB (asterisks) and PAGB stars (open circles). The mass-loss rates derived from the observed rotational transitions of CO at mm wavelengths for some of the AGB and PAGB stars in our sample (filled diamonds) are also shown for comparison.

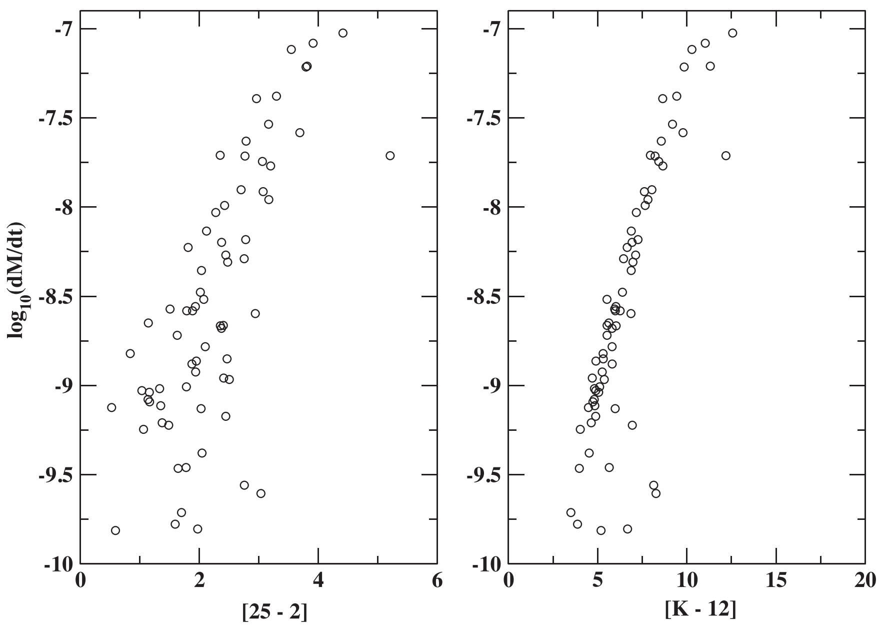

Figure 10. Plot of the dust mass-loss rate obtained using the relation from Lagadec et al. (2008) with the mass-loss indexes $[25-2]$ and $[K-12]$ for the sample PAGB stars (open circles).

the superwind phase alone, so intense mass loss should continue beyond the superwind phase before the star becomes a PN, thus explaining our SED model results. Hrivnak & Bieging (2005) had suggested intense mass loss during the PAGB phase, responsible for the steeper density law for fitting their observed CO rotational line profiles.

5.3 Trends in PAH modes with evolution

Here we examine the trends in the strength of the PAH emission modes with the stellar effective temperature T_*. T_* is used to represent the evolutionary stage of the sources considered in the present study; the higher the value, the more advanced the evolution of the source. Interesting correlations were obtained between the strengths of PAH spectral features with the physical and circumstellar parameters of the PAGB candidates by Peeters et al. (2002), Sloan et al. (2005), Bernard-Salas et al. (2009) and Hony et al. (2001). In this section, we examine the present sample of PAGB objects for such possible correlations with stellar temperature and other parameters that characterize the circumstellar envelope.

First, we examined the correlation between intensity ratios $I(7.7)/I(11.2)$ and $I(6.2)/I(11.2)$. Each of these ratios is known to

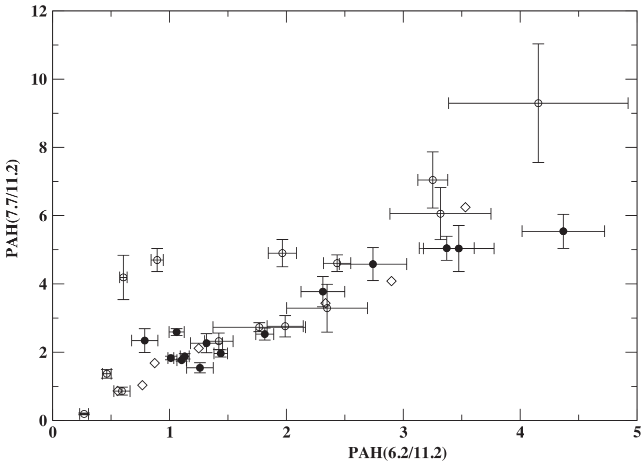

Figure 11. Plot of PAH mode flux ratio [7.7]/[11.2] versus [6.2]/[11.2] for PAGB stars. The open circles represent the PAGB stars in our sample, while the filled circles represent PNe in the Large Magellanic Cloud (LMC) and Small Magellanic Cloud (SMC) and the open diamonds represent the same in our Milky Way galaxy obtained from Bernard-Salas et al. (2009), shown for comparison.

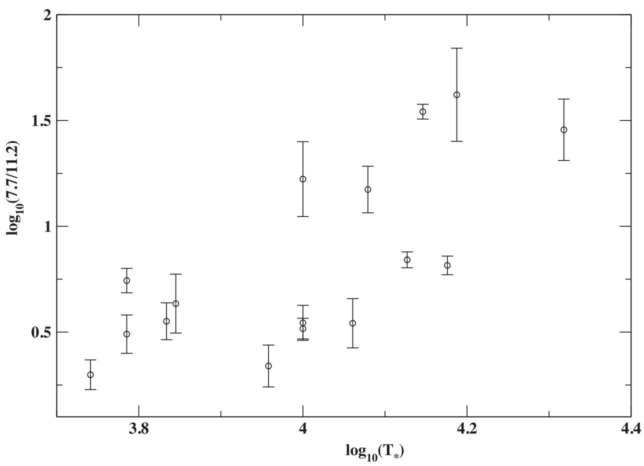

Figure 12. Plot of PAH mode ratio EW[7.7]/EW[11.2] versus effective temperature T_* for PAGB stars.

indicate the ionization fraction in PAH molecules (Galliano et al. 2008). Fig. 11 shows a plot of these intensity ratios indicating a positive correlation, a trend that was earlier shown by Cerrigone et al. (2009).

We have also studied the relative dominance of C–C stretching, C–H in-plane bending modes (e.g. 7.7 μm) and C–H out-of-plane (e.g. 11.2 μm) modes as the stars evolve. It may be noted that we have used the equivalent width (EW) as the measure of the strength of the PAH feature, instead of the feature intensity used by other authors (e.g. Cerrigone et al. 2009; Zhang et al. 2010). We have found that using EW yielded essentially the same results as using the intensity of spectral features. Figs 12 and 13 show the ratio of the EWs of the PAH features [7.7]/[11.2] versus T_* and the radius of the central source r_c respectively. The PAH feature at 7.7 μm represents the C–C stretching and C–H in-plane bending modes and the 11.2-μm feature represents the solo C–H out-of-plane bending modes. One may notice a tendency of increasing ratio with T_*, indicating the dominance of C–C stretching and C–H in-plane bending modes as the objects evolve, while a decreasing tendency may be noticed

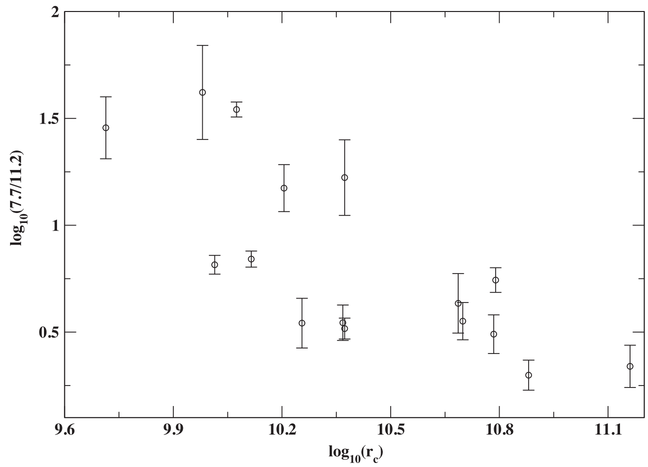

Figure 13. Plot of PAH mode ratio EW[7.7]/EW[11.2] versus the radius of the central source r_c for PAGB stars.

with r_c. As mentioned earlier, one may also conclude from this plot that stars showing ratio [7.7/11.2] > 1 have a higher fraction of ionized PAHs than those with a lower ratio.

In their study of a few PAGB candidates, Zhang et al. (2010) showed that the ratio [12.6/11.2] tends to decrease with the central star temperature, indicating that the solo C–H modes at 11.2 μm become more and more predominant over the duo, trio or quarto modes at 12–13 μm. This is suggestive of the possibility that the solo C–H out-of-plane bending modes get stronger as stars evolve to PNe (Kwok 2004). We also found in the present sample that the ratio indicated a decreasing trend with T_* (not shown here). The ratio is less than 1 for nearly all sources that showed PAH bands, suggesting that solo modes dominate over duo and trio modes. Our result is in agreement with Zhang et al. (2010). In most cases of PNe in their sample, Hony et al. (2001) found that the ratio as a function of the hard radiation field remained less than 1.

We have also seen whether there is a trend between the central source temperature and the plateau region 16–20 μm representing the blended features of in-plane or out-of-plane C–C–C bending modes normalized with the 11.2-μm solo band. A decreasing trend of the mode with T_* was noticed (not shown here).

Sloan et al. (2007) showed that the peak wavelength of the 11.2-μm feature changes with T_* for a small sample of carbon stars. We verified this result with our sample. Fig. 14 shows a plot of peak wavelengths of the 6.2-, 7.7- and 11.2-μm features with T_* (see Table 2). One may notice, in general, a shift towards shorter wavelengths with increasing T_*, up to a value of 10^4 K, in agreement with Zhang et al. (2010). Sloan et al. (2007) assume that PAH clusters are embedded in a matrix of aliphatic groups. When such hydrogenated amorphous carbon (HAC) material is exposed to hard radiation, the aliphatic bonds break down progressively, leading to positional shifts of PAH features (for details see Sloan et al. 2007).

6 IDENTIFICATION OF TRANSITION OBJECTS

The transition process from the post-AGB to PN phase still remains elusive in stellar evolution. After the termination of high AGB mass loss, the circumstellar envelopes expand and cool and the effective temperature of the central star increases to ionize the circumstellar material towards the end of the post-AGB phase (Kwok & Feldman 1981; Kwok & Bignell 1984). Mid-IR fine-structure lines suffer

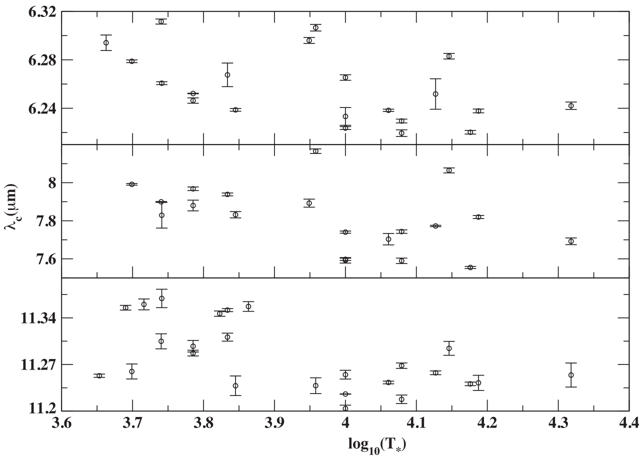

Figure 14. Plot of the peak wavelength of the PAH features at 6.2, 7.7 and 11.2 µm versus the photospheric temperature T_* for PAGB stars.

less dust extinction compared with optical and UV emission lines and hence are easier to detect. However, not all PAGB objects show these emission lines indicating their transition nature; a possible explanation is in order. The morphologies of PAGB dust shells are believed to be predominantly axisymmetric (Ueta, Meixner & Bobrowsky 2000) and interact with the PAGB winds to form aspherical PN shells. Mid-infrared imaging of PAGB sources shows a central dust torus around the central source (Ueta et al. 2001). The mid-IR morphologies of the circumstellar shell are characterized into two groups: namely toroidal and core/elliptical (Meixner et al. 1999). The toroidal dust shells have very low optical depth and the starlight can scatter in all directions. In the case of elliptical mid-IR shells, the optical depth is high and the starlight can escape only through the bicone opening of the dust shell, making bipolar nebulosities. The fine-structure emission lines are believed to arise from irradiated central torus atmospheres. In order to observe these lines, the inclination of the source and the optical depth along the line of sight play a crucial role. If the source is viewed pole-on, then the line-of-sight optical depth is highest from the circumstellar shells and makes detection difficult. When observed edge-on, one may view the interaction of fast winds with the dense equatorial torus. Hence the detection of these lines depends on the morphology and inclination of the source.

Fig. 15 represents *Spitzer* IRS spectra of transition objects with hot cores ionizing the circumstellar matter, thereby making a transition from PAGB to PN phases, showing low- and high-excitation fine-structure lines. There are around 31 objects in the sample that may be termed as hot objects having $T_* \geq 10^4$ K, but only nine of these show fine-structure lines of Ne. The IRS spectra of the PAGB candidates IRAS 01005+7910, IRAS 21546+4721 and IRAS 22023+5429 showed PAH emission in addition to [Ne II]. Among the other PAGB candidates showing transition behaviour, IRAS 10211−5922, IRAS 17381−1616 and IRAS 19590−1249 showed silicate in emission. The source IRAS 10211−5922 shows [Ni I], [Ni II], [Ar II], [Co I] and [C II] in addition to the [Ne II] line, thereby suggesting its advanced stage of evolution among the other candidates. Also, IRAS 17287−3443 and IRAS 17311−4924 show peculiar dust properties in addition to the fine-structure lines. IRAS 17311−4924 shows high-excitation lines of [Ar III], [S IV] and [Ne III] in addition to the [Ni I] lines. It also shows faint emission of the [Ne II] line at a relatively lower S/N. Further, it shows a rising mid-infrared continuum (near the [S IV] line), possibly due to very small grains (VSGs) that can survive close to the hot source (Lebouteiller et al. 2007). In the light of this fine-structure line emission and the contribution due to VSGs, IRAS 17311−4924 might be a high-excitation transition object. The sources IRAS 20462+3416 and IRAS 22023+5429 are mixed-chemistry objects with [Ne II] emission. As argued above, the reason for fewer candidates showing [Ne II] emission could be due to orientation effects and the deeply embedded nature of the elliptical dust shells. Our SED model of sources with hot central temperatures also shows large $\tau_{0.55}$ values. Even with the uncertainty associated with model $\tau_{0.55}$ values, the trend is compelling: those that showed a [Ne II] line have much lower $\tau_{0.55}$ values, with the exception of IRAS 17287−3443, compared with those that did not.

7 DETECTION OF FULLERENE IN IRAS 21546+4721

Fullerene molecules (C_{60}) are large molecules made of carbon hexagons and pentagons that are organized in the shape of a hollow sphere (Kroto et al. 1985; Kroto 1988; Curl & Smalley 1988; Krätschmer et al. 1990). Fullerenes are not only formed in hot and dense envelopes of evolved stars, but also identified in the tenuous and cold environment of interstellar clouds illuminated by strong ultraviolet radiation. The formation mechanism of this molecule in space is still unclear. The observed abundance of fullerene challenges the standard ion–molecule or grain-surface chemistry formation routes. Laboratory results showed an inhibition in fullerene formation with the presence of hydrogen, while supporting the formation of PAH (de Vries et al. 1993). Another mechanism that is getting much interest in recent times is the top-down model, whereby photochemical processing of hydrogenated amorphous carbon (HAC) grains results in the formation of PAH and fullerene (García-Hernandez et al. 2010; Micelotta et al. 2012; Bernard-Salas et al. 2012). The mid-IR vibrational modes of C_{60} lie at 18.9, 17.4, 8.5 and 7.0 µm. The first astronomical detection of fullerene in the circumstellar environment of a young PN, Tc1, was made by Cami et al. (2010). Fullerene was detected in young carbon-rich PNe in the Milky Way galaxy (Bernard-Salas et al. 2012; Otsuka et al. 2014) and Magellanic Clouds (Bernard-Salas et al. 2012). Bernard-Salas et al. (2012) suggested that physical conditions found in these PNe could favour the formation of fullerene. C_{60} had been detected in a few post-AGB binary stars earlier by Roberts, Smith & Sarre (2012) and Gielen et al. (2011) in a mixed oxygen–carbon rich environment. Zhang & Kwok (2011) had detected C_{60} in the PPN IRAS 01005+7910. All in all, there are very few detections of C_{60} in late-type stars. We searched carefully for C_{60} vibrational modes in the *Spitzer* IRS spectra of PAGB candidates in our sample. We detected vibrational modes of C_{60} for the first time in one of the PAGB candidates, IRAS 21546+4721. To the best of our knowledge, this is the first detection of C_{60} in this source and one of the very few detections reported yet. Fig. 16 shows the vibrational modes of C_{60} observed in IRAS 21546+4721 compared with those of IRAS 01005+7910. The spectra of both objects also show the C–C stretching and C–H bending modes of vibration of PAH. The vibrational transitions of fullerene at 17.4 and 18.9 µm are very clear in both cases, while those at 7.0 and 8.5 µm are blended with [Ar II] and PAH, respectively. Modelling of the spectral energy distribution indicates a photospheric temperature greater than 10^4 K for both sources. The presence of a forbidden line of [Ne II] in IRAS 21546+4721 further indicates its advanced stage of evolution. Also, both spectra show strong emission of a 30-µm feature (see Fig. 16) that is attributed to MgS (Goebel & Moseley 1985) or a carbonaceous compound (Zhang, Jiang & Li 2009). Otsuka et al. (2014) found the presence of a 30-µm feature in all their sample

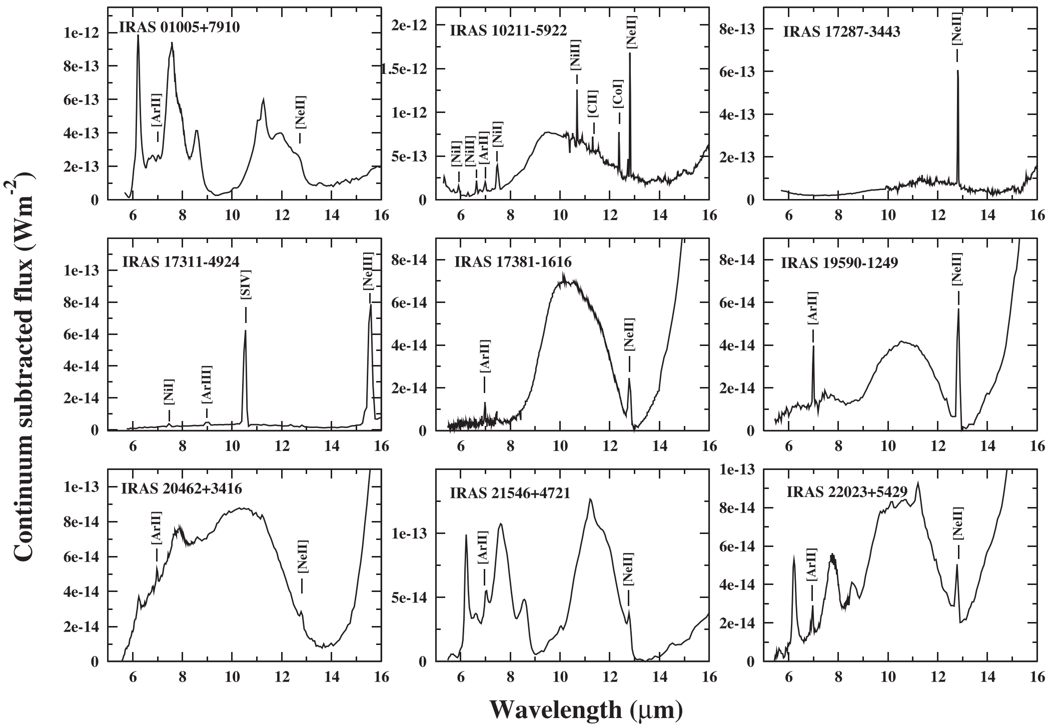

Figure 15. Transition objects from our sample showing prominent low- and high-excitation fine-structure lines.

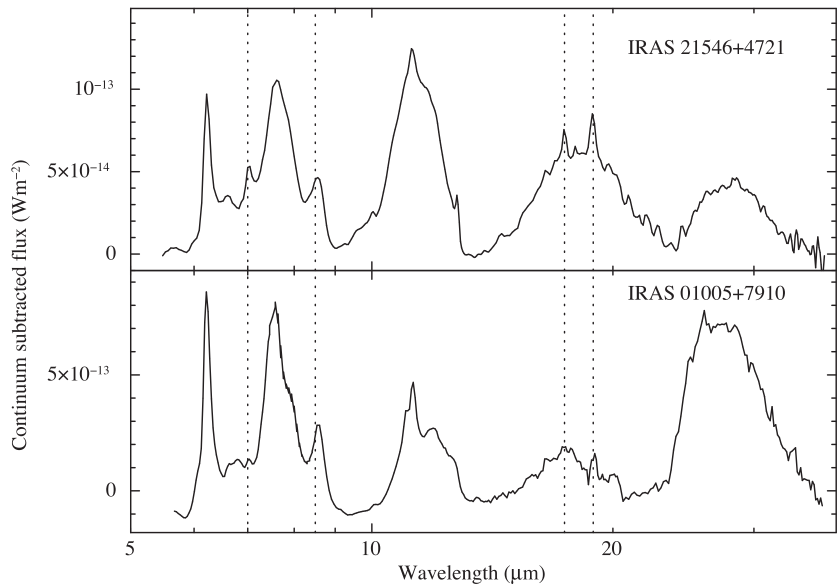

Figure 16. *Spitzer* IRS spectra of PAGB candidates IRAS 21546+4721 and IRAS 01005+7910, showing vibrational modes of C_{60} fullerene.

Galactic PNe that have fullerene. Further, the absence of a 21-µm feature in the mid-IR spectra of IRAS 21546+4721 and IRAS 01005+7910 rules out the possibility of fullerene as a carrier for this feature, as suggested by Justtanont et al. (1996) and Garcia et al. (1999).

8 CONCLUSIONS

(i) Based on our analysis of *Spitzer* mid-infrared spectra of a fairly large sample of PAGB stars, we have broadly classified them in to those having

(a) strong/weak or blended PAH,
(b) silicate emission, in some cases along with PAH features,
(c) silicate absorption,
(d) a prominent broad bump around 11 µm and
(e) nearly featureless spectra.

(ii) The SED modelling of the PAGB objects shows that the temperature of the inner dust shell decreases with increasing inner radius r_1, while the ratio r_1/r_c shows an increasing tendency with stellar photospheric temperature; the total mass-loss rate correlates negatively with dust temperature and shows an increasing tendency with $\tau_{0.55}$.

(iii) The post-AGB mass-loss rates obtained from the SED models are higher than those of the AGB and show a correlation with the mass-loss indices [$K - 12$] and [25 − 2]. Dust mass-loss rates obtained independently from the IR colours and *Spitzer* spectra also followed a similar trend.

(iv) The PAGB objects that show PAH emission features in the range 5–20 μm indicate the onset of UV radiation from the central star and hence represent an advanced stage of evolution. The ratio of the observed strength of the 7.7- and 11.2-μm PAH features showed an increasing trend with T_*, while decreasing with r_c. The peak wavelengths of the 6.2-, 7.7- and 11.2-μm features seem to shift towards shorter wavelengths with increasing T_*.

(v) Nine objects in our sample showed a fine-structure line of Ne, indicating their transition nature from PAGB to PNe with the onset of ionization.

(vi) Fullerene was detected for the first time in the PAGB star IRAS 21546+4721.

ACKNOWLEDGEMENTS

This research was supported by the Department of Space, Government of India. The research has made use of the SIMBAD data base operated at CDS, Strasbourg, France; the NASA/IPAC Infrared Science Archive, which is operated by the Jet Propulsion Laboratory, California Institute of Technology, under contract with the National Aeronautics and Space Administration, USA; and the data products from the Two Micron All Sky Survey, which is a joint project of the University of Massachusetts and the Infrared Processing and Analysis Center/California Institute of Technology, funded by the National Aeronautics and Space Administration and the National Science Foundation. We acknowledge the DUSTY team for making their codes available for the astronomy community. We sincerely thank the anonymous referee for very useful comments, which improved the quality of the article.

REFERENCES

Allen C. W., 2000, in Cox A. N., ed., Astrophysical Quantities. Springer-Verlag, Heidelberg

Anandarao B. G., Pottasch S. R., Vaidya D. B., 1993, A&A, 273, 570

Benjamin R. A. et al., 2003, PASP, 115, 953

Bernard-Salas J., Peeters E., Sloan G. C., Gutenkunst S., Matsuura M., Tielens A. G. G. M., Zijlstra A. A., Houck J. R., 2009, ApJ, 699, 1541

Bernard-Salas J., Cami J., Peeters E., Jones A. P., Micelotta E. R., Groenewegen M. A. T., 2012, ApJ, 757, 41

Blasberger A., Behar E., Perets H. B., Brosch N., Tielens A. G. G. M., 2017, ApJ, 836, 173

Bouwman J., Meeus G., de Koter A., Hony S., Dominik C., Waters L. B. F. M., 2001, A&A, 375, 950

Bujarrabal V., Castro-Carrizo A., Alcolea J., Sanchez Contreras C., 2001, A&A, 377, 868

Cami J., Bernard-Salas J., Peeters E., Malek S. E., 2010, Science, 329, 1180

Cerrigone L., Hora J. L., Umana G., Trigilio C., 2009, ApJ, 703, 585

Chalabaev A., Maillard J. P., 1983, A&A, 127, 279

Curl R. F., Smalley R. E., 1988, Science, 242, 1017

de Vries M. S., Reihs K., Wendt H. R., Golden W. G., Hunziker H. E., Fleming R., Peterson E., Chang S., 1993, Geochim. Cosmochim. Acta, 57, 933

de Vries B. L., Blommaert J. A. D. L., Waters L. B. F. M., Waelkens C., Min M., Lombaert R., Van Winckel H., 2014, A&A, 561, A75

de Vries B. L., Maaskant K. M., Min M., Lombaert R., Waters L. B. F. M., Blommaert J. A. D. L., 2015, A&A, 576, A98

Duley W. W., 2000, ApJ, 528, 841

Egan M. P., Price S. D., Kraemer K. E., 2003, BAAS, 35, 1301

Galliano F., Madden S. C., Tielens A. G. G. M., Peeters E., Jones A. P., 2008, ApJ, 679, 310

García-Lario P., Perea Calderón J. V., 2003, in Gry C., Peschke S., Matagne J., Garcia-Lario P., Lovente R., Salama A., eds, Exploiting the ISO Data Archive: Infrared Astronomy in the Internet Age, ESA SP-511. ESA, Noordwijk, p. 97

Garcia-Lario P., Manchado A., Ulla A., Manteiga M., 1999, ApJ, 513, 941

García-Hernández D. A., Manchado A., García-Lario P., Stanghellini L., Villaver E., Shaw R. A., Szczerba R., Perea-Calderón J. V., 2010, ApJ, 724, L39

Gielen C., Cami J., Bouwman J., Peeters E., Min M., 2011, A&A, 536, A54

Goebel J. H., Moseley S. H., 1985, ApJ, 290, L35

Guzman-Ramirez L. et al., 2015, MNRAS, 451, L1

Helou G., Walker D. W., 1988, Infrared astronomical satellite (IRAS) catalogs and atlases, 7, 1

Hony S., Van Kerckhoven C., Peeters E., Tielens A. G. G. M., Hudgins D. M., Allamandola L. J., 2001, A&A, 370, 1030

Hoogzaad S. N., Molster F. J., Dominik C., Waters L. B. F. M., Barlow M. J., de Koter A., 2002, A&A, 389, 547

Houck J. R. et al., 2004, in Mather J. C., ed., Proc. SPIE Conf. Ser. Vol. 5487, Optical, Infrared, and Millimeter Space Telescopes. SPIE, Bellingham, p. 62

Hrivnak B. J., Bieging J. H., 2005, ApJ, 624, 331

Hrivnak B. J., Kwok S., 1999, ApJ, 513, 869

Hrivnak B. J., Volk K., Kwok S., 2000, ApJ, 535, 275

Hrivnak B. J., Lu W., Nault K. A., 2015, AJ, 149, 184

Ishihara D., Onaka T., Kataza H., 2010, A&A, 514, 14

Ivezic Z., Elitzur M., 1995, ApJ, 445, 415

Ivezic Z., Elitzur M., 1997, MNRAS, 287, 799

Ivezic Z., Nenkova M., Elitzur M., 1999, User Manual for dusty, University of Kentucky Internal Report, accessible at http://www.pa.uky.edu/moshe/dusty

Jaeger C., Molster F. J., Dorschner J., Henning T., Mutschke H., Waters L. B. F. M., 1998, A&A, 339, 904

Justtanont K., Barlow M. J., Skinner C. J., Roche P. F., Aitken D. K., Smith C. H., 1996, A&A, 309, 612

Kelly D. M., Hrivnak B. J., 2005, ApJ, 629, 1040

Krätschmer W., Lamb L. D., Fostiropoulos K., Huffman D. R., 1990, Nature, 347, 354

Kroto H., 1988, Science, 242, 1139

Kroto H. W., Heath J. R., Obrien S. C., Curl R. F., Smalley R. E., 1985, Nature, 318, 162

Kwok S., 2004, Nature, 430, 985

Kwok S., 2007, The Origin and Evolution of Planetary Nebulae. Cambridge University Press, Cambridge, UK

Kwok S., Bignell R. C., 1984, ApJ, 276, 544

Kwok S., Feldman P. A., 1981, ApJ, 247, L67

Kwok S., Volk K., Hrivnak B. J., 1999, A&A, 350, L35

Lagadec E., Zijlstra A. A., Matsuura M., Menzies J. W., van Loon J. T., Whitelock P. A., 2008, MNRAS, 383, 399

Lamers H. J. G. L. M., Cassinelli J. P., 1999, Introduction to Stellar Winds. Cambridge Univ. Press, Cambridge, UK

Lang K. R., 2006, Astrophysical Formulae. Springer-Verlag, Heidelberg

Le Bertre T., Winters J. M., 1998, A&A, 334, 173

Lebouteiller V., Brandl B., Bernard-Salas J., Devost D., Houck J. R., 2007, ApJ, 665, 390

Li A., Draine B. T., 2001, ApJ, 554, 778

Likkel L., Forveille T., Omont A., Morris M., 1991, A&A, 246, 153

Mathis J. S., Rumpl W., Nordsieck K. H., 1977, ApJ, 217, 425

Meixner M., Skinner C. J., Graham J. R., Keto E., Jernigan J. G., Arens J. F., 1997, ApJ, 482, 897

Meixner M. et al., 1999, ApJS, 122, 221

Micelotta E. R., Jones A. P., Cami J., Peeters E., Bernard-Salas J., Fanchini G., 2012, ApJ, 761, 35

Mishra A., Li A., Jiang B. W., 2016, ApJ, 825, 68

Omont A., Loup C., Forveille T., te Lintel Hekkert P., Habing H., Sivagnanam P., 1993, A&A, 267, 515

Otsuka M., Kemper F., Cami J., Peeters E., Bernard-Salas J., 2014, MNRAS, 437, 2577
Peeters E., Hony S., Van Kerckhoven C., Tielens A. G. G. M., Allamandola L. J., Hudgins D. M., Bauschlicher C. W., 2002, A&A, 390, 1089
Peeters E., Bauschlicher C. W., Jr, Allamandola L. J., Tielens A. G. G. M., Ricca A., Wolfire M. G., 2017, ApJ, 836, 198
Posch T., Mutschke H., Andersen A., 2004, ApJ, 616, 1167
Roberts K. R. G., Smith K. T., Sarre P. J., 2012, MNRAS, 421, 3277
Salpeter E. E., 1977, Annu. Rev. Astron. Astrophys., 15, 267
Schoenberner D., 1983, ApJ, 272, 708
Sedlmayr E., Winters J. M., 2000, in Wing R. F., ed., Proc. IAU Symp. 177, The Carbon Star Phenomenon. Kluwer, Dordrecht, p. 337
Skrutskie M. F. et al., 2006, AJ, 131, 1163
Sloan G. C., Kraemer K. E., Price S. D., Shipman R. F., 2003, ApJS, 147, 379
Sloan G. C. et al., 2005, ApJ, 632, 956
Sloan G. C. et al., 2007, ApJ, 664, 1144
Smith J. D. T. et al., 2007, ApJ, 656, 770
Speck A. K., Hofmeister A. M., 2004, ApJ, 600, 986
Speck A. K., Thompson G. D., Hofmeister A. M., 2005, ApJ, 634, 426
Spoon H. W. W., Marshall J. A., Houck J. R., Elitzur M., Hao L., Armus L., Brandl B. R., Charmandaris V., 2007, ApJ, 654, L49
Suarez O., Garcia-Lario P., Manchado A., Monteiga M., Ulla A., Pottasch S. R., 2006, A&A, 458, 173
Szczerba R., Siodmiak N., Stasinska G., Borkowski J., 2007, A&A, 469, 799
Tielens A. G. G. M., 2005, The Physics and Chemistry of the Interstellar Medium. Cambridge Univ. Press, Cambridge, p. 173
Uchida K. I., Sellgren K., Werner M. W., Houdashelt M. L., 2000, ApJ, 530, 817
Ueta T., Meixner M., Bobrowsky M., 2000, ApJ, 528, 861
Ueta T. et al., 2001, ApJ, 557, 831
van der Veen W. E. C. J., Habing H. J., 1988, A&A, 194, 125
van Winckel H., 2003, ARAA, 41, 391
Vassiliadis E., Wood P. R., 1994, ApJS, 92, 125
Venkata Raman V., Anandarao B. G., 2008, MNRAS, 385, 1076
von Helden G., Tielens A. G. G. M., van Heijnsbergen D., Duncan M. A., Hony S., Waters L. B. F. M., Meijer G., 2000, Science, 288, 313
Waelkens C., Waters R. B. F. M., 2003, in Habing H. J., Olofsson H., eds, Asymptotic giant branch stars, Astronomy and astrophysics library, Springer-Verlag, New York, p. 519
Waters L. B. F. M. et al., 1998, Nature, 391, 868
Woitke P., Goeres A., Sedlmayr E., 1996, A&A, 313, 217
Woodsworth A. W., Kwok S., Chen S. J., 1990, A&A, 228, 503
Zhang Y., Kwok S., 2011, ApJ, 730, 126
Zhang K., Jiang B. W., Li A., 2009, ApJ, 702, 680
Zhang Y., Kwok S., Hrivnak B. J., 2010, ApJ, 725, 990

APPENDIX A: CONTINUUM-SUBTRACTED SPITZER IRS SPECTRA OF SAMPLE PAGB STARS

The continuum-subtracted *Spitzer* IRS spectra in the wavelength region 5–38 μm are shown in Figs A1–A7, arranged categorywise (see text for details).

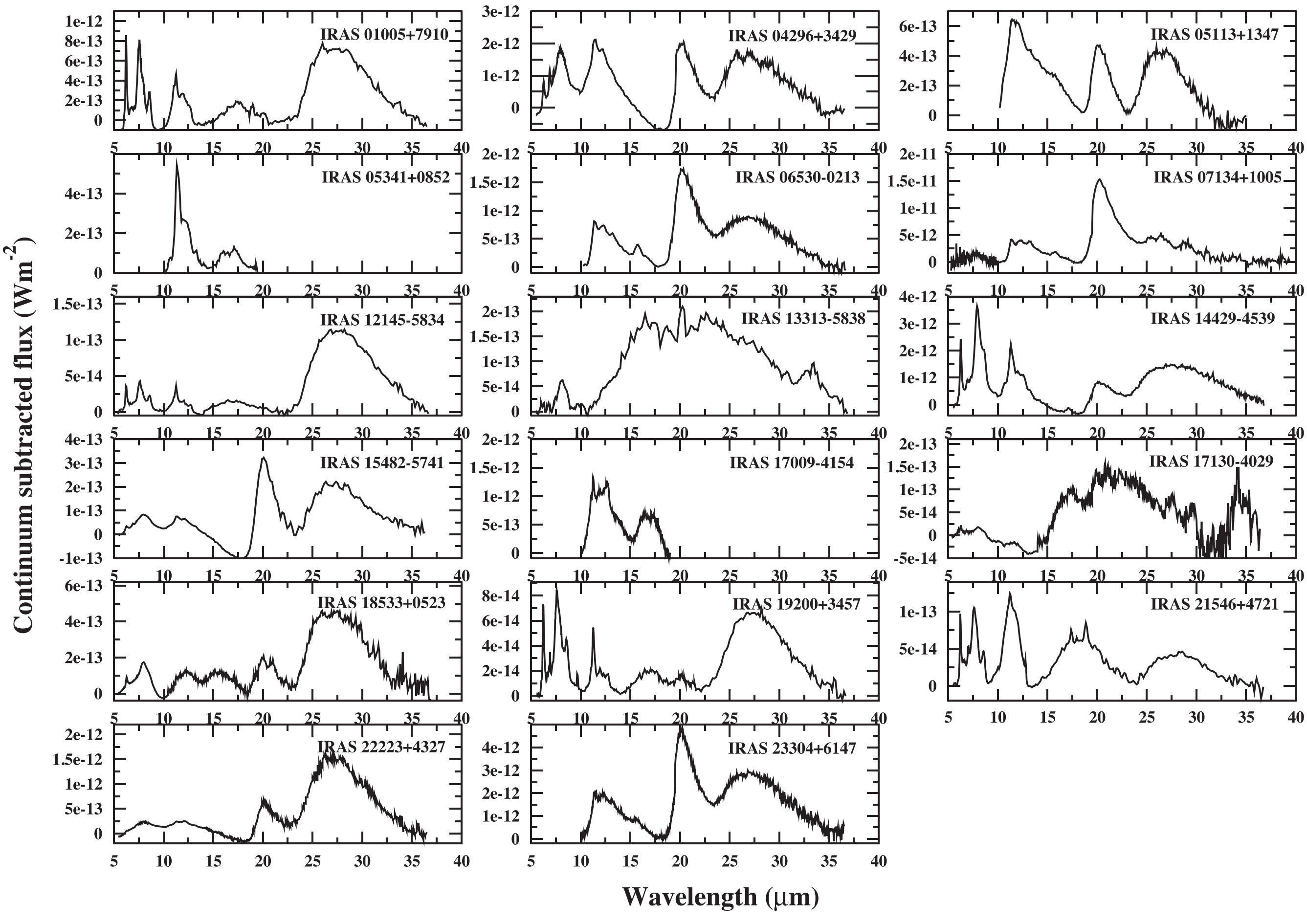

Figure A1. Continuum-subtracted *Spitzer* IRS spectra for sources with PAH emission (classes 1a, 1b, 1c).

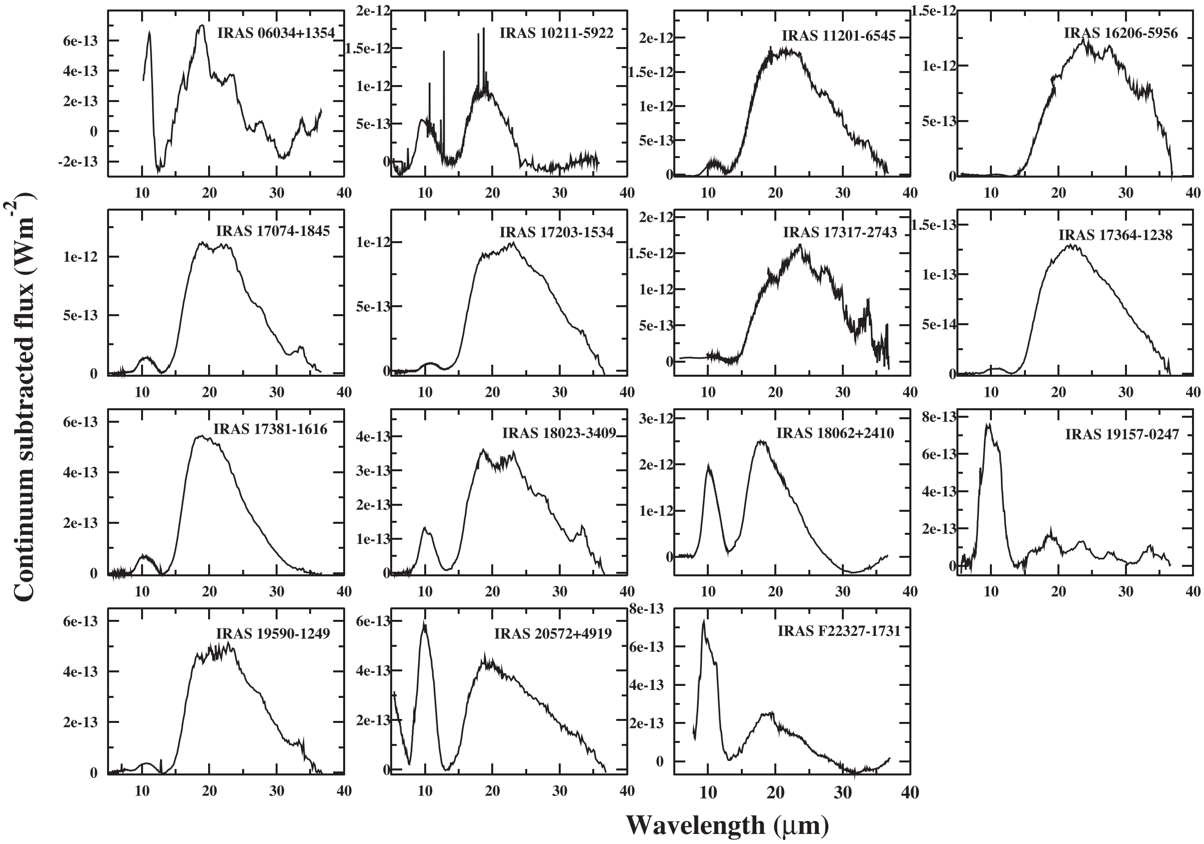

Figure A2. Continuum-subtracted *Spitzer* IRS spectra for sources with silicate emission (class 2a).

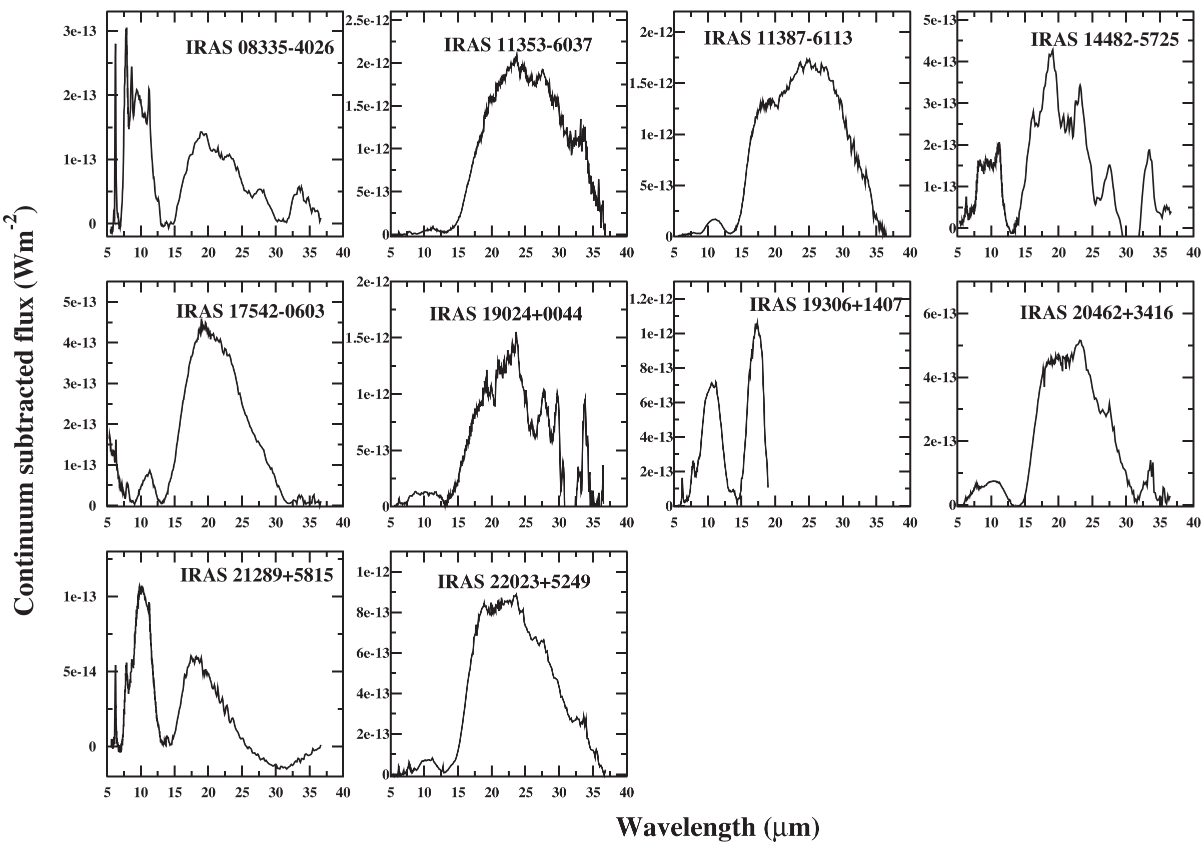

Figure A3. Continuum-subtracted *Spitzer* IRS spectra for sources with PAH and silicate emission (class 2b).

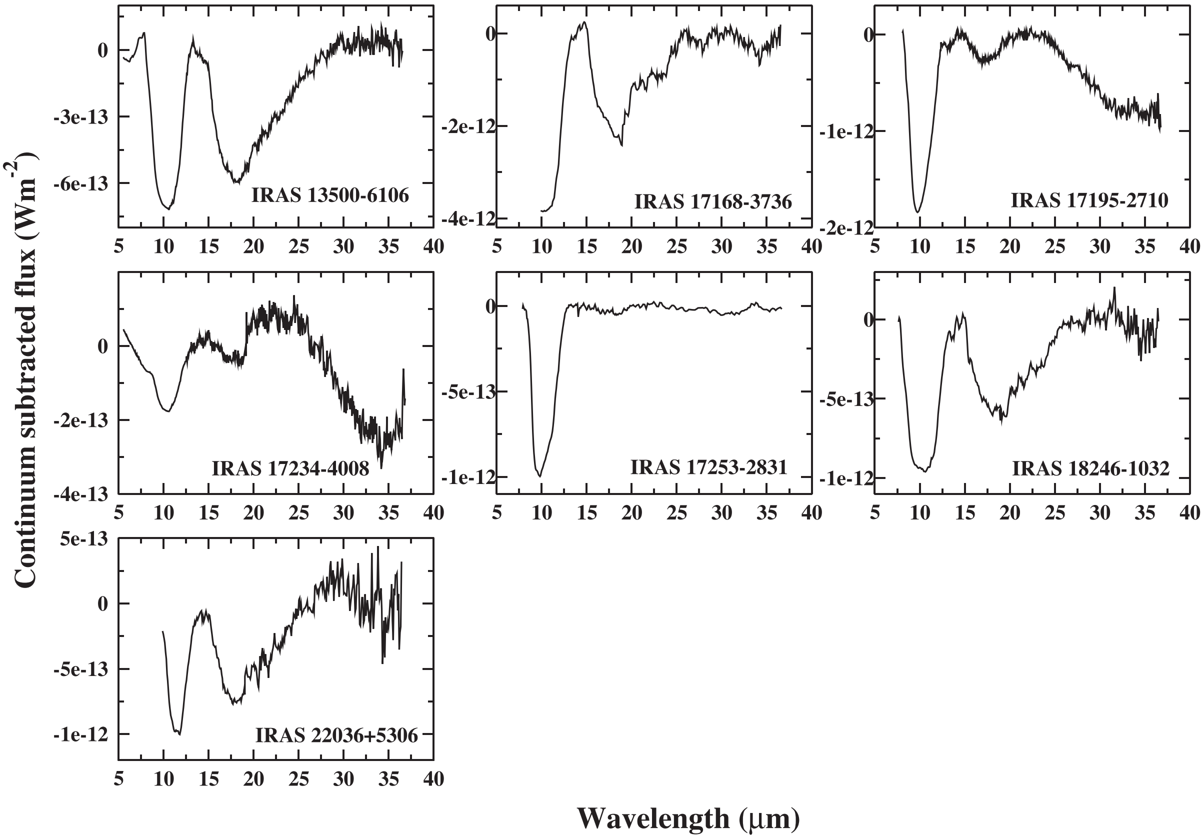

Figure A4. Continuum-subtracted *Spitzer* IRS spectra for sources with silicate absorption (class 3).

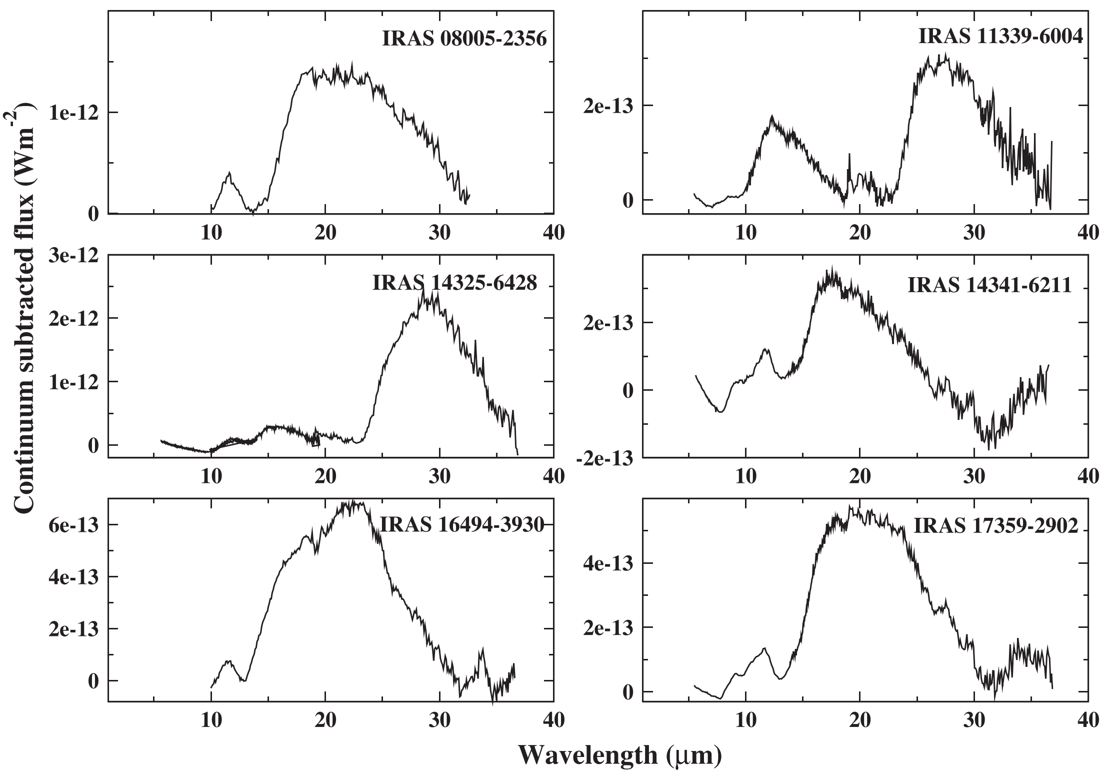

Figure A5. Continuum-subtracted *Spitzer* IRS spectra for sources with broad 11-μm emission (class 4).

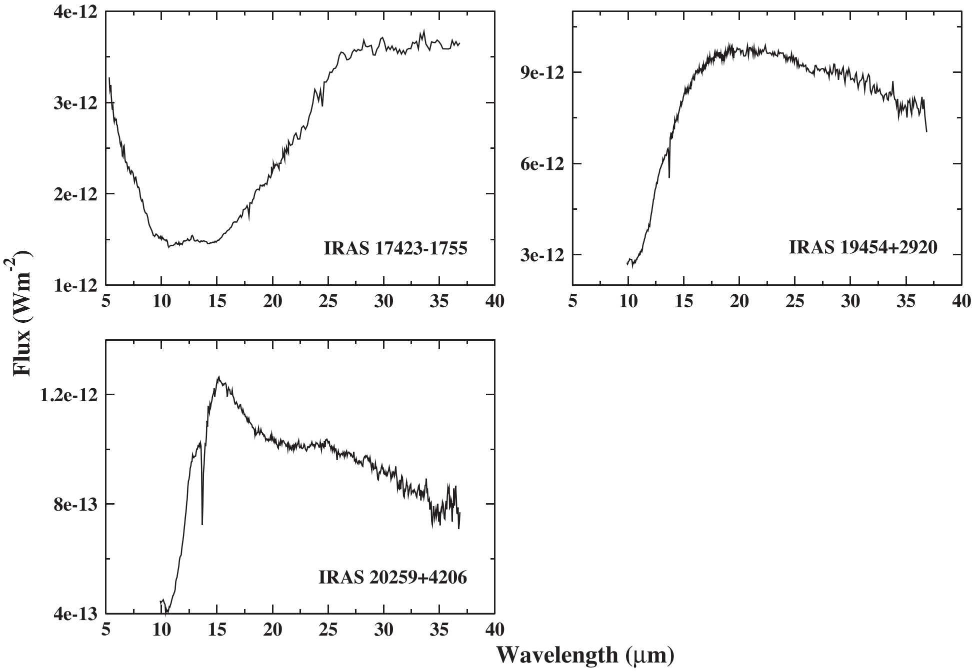

Figure A6. *Spitzer* IRS spectra for sources with featureless dust continuum (class 5).

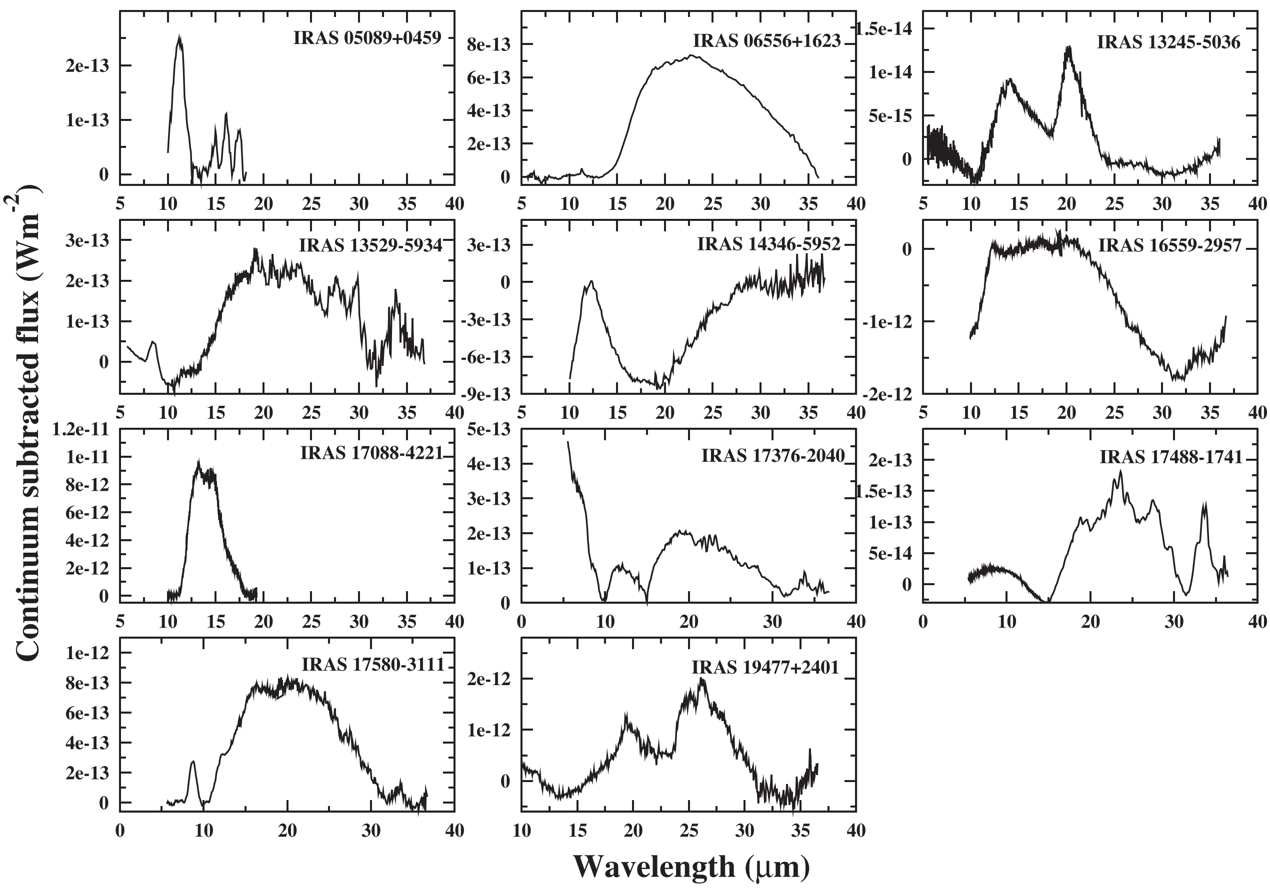

Figure A7. Continuum-subtracted *Spitzer* IRS spectra for sources that do not fall in the proposed classification scheme.

This paper has been typeset from a TEX/LATEX file prepared by the author.